2011

Application of the TDMA Technique Toward the Size and Charge Distribution Measurement of Graphite, Gold, Palladium, and Silver Aerosols

Matthew Paul Simones
Minnesota State University - Mankato

Recommended Citation

Simones, Matthew Paul, "Application of the TDMA Technique Toward the Size and Charge Distribution Measurement of Graphite, Gold, Palladium, and Silver Aerosols" (2011). *Theses, Dissertations, and Other Capstone Projects.* Paper 183.

Application of the TDMA Technique Toward the Size and Charge Distribution Measurement of Graphite, Gold, Palladium, and Silver Aerosols

By
Matthew Paul Simones

A Thesis Submitted in Partial Fulfillment of the
Requirements for Masters of Science
In
Mechanical Engineering

Minnesota State University, Mankato
Mankato, MN

May 2011

Application of the TDMA Technique Toward the Size and Charge Distribution Measurement of Graphite, Gold, Palladium, and Silver Aerosols

Matthew Paul Simones

This thesis has been examined and approved by the following members of the thesis committee.

Dr. Patrick Tebbe, Advisor

Dr. Saeed Moaveni

Dr. Sudarshan Loyalka

Acknowledgements

First and foremost I would like to thank my graduate committee for their guidance and patience throughout the duration of this project. I would also like to thank my advisor Dr. Patrick Tebbe for introducing me to the Nuclear Science and Engineering Institute (NSEI) at the University of Missouri where the following experimental work was completed, and Dr. Sudarshan Loyalka for the opportunity to join NSEI both as a Masters student and a PhD candidate.

Special thanks to Dr. Veera Rajesh Gutti for his help with various tasks and instrument training, in addition to providing TEM images, Fluent CFD computations, and help with Mathematica programming. I would also like to thank Dr. Ryan Meyer for his help with electrical modifications of the aerosol equipment and Dr. Zebadiah Smith for his help with Mathematica output formatting. Thanks are all also due to the Missouri Space Grant Consortium who provided partial funding during my visit to NSEI during the summer of 2009.

Finally, this thesis is dedicated to my parents Paul and Patti who have always been supportive throughout my many endeavors, and to my fiancée Brooke who remains both supportive and patient as I complete my academic goals.

Application of the TDMA Technique Toward the Size and Charge Distribution Measurement of Graphite, Gold, Palladium, and Silver Aerosols

Matthew Paul Simones

Mechanical Engineering
Minnesota State University, Mankato
Mankato, MN
2011

Abstract

The knowledge of charge distributions among aerosol particles has been an important topic for many years because of the strong electrostatic interactions which can greatly influence aerosol transport and evolution. Theoretical models have been developed although experimental verification has been limited because of the difficulty in measuring charged aerosols. Recently a method utilizing a tandem differential mobility analyzer (TDMA) has been shown to be applicable toward measuring both the size and charge distributions of nanosized combustion aerosols. The goal of this work is on further exploration of this method toward the measurement of non-combustion aerosols and in particular those associated with very high temperature reactors (VHTRs). The complete bipolar charge and size distributions of spark generated graphite, gold, silver, and palladium aerosol have been measured with a TDMA apparatus assembled and calibrated during this study. In addition, an electrostatic precipitator has been designed and constructed for measuring the size distributions of neutrally charged particles associated with these aerosols. The results show charge asymmetry in all measured aerosols with higher concentrations of positively charged particles than negative at the same charge level. These results differ from equilibrium charge distributions of both Boltzmann and

Fuchs showing that charge equilibrium may not always be an appropriate assumption. The TDMA technique should find applications in characterizing VHTR aerosols and rate processes such as coagulation, deposition, and resuspension which will be important for both reactor design, and accident modeling and simulation.

Table of Contents

List of Figures

List of Tables

Symbols

a	Intercept determined from linear regression
A	Cross-sectional area (m^2)
b	Gradient determined from linear regression
c_p	Specific heat capacity at constant pressure (J kg^{-1} K^{-1})
$C_c\left(d_p\right)$	Cunningham slip correction factor $= 1 + Kn\left(1.142 + 0.558e^{\left(\frac{-.999}{Kn}\right)}\right)$
d	ESP collector plate separation (m)
d_p	Particle diameter (m)
$\bar{d}_p$	Mean particle diameter associated with $\bar{Z}_p$ (m)
D_H	Hydraulic diameter $= \frac{4A}{P}$ (m)
$\tilde{D}_p$	Dimensionless particle diameter $= \frac{d_p}{\bar{d}_p}$
$\tilde{D}_{pg}$	Geometric mean of Ω in $\tilde{D}_p$ space
e	Elementary unit of charge $= 1.602 \times 10^{-19}$ (C)
F_D	Aerodynamic drag force on particle (N)
F_E	Electrostatic force on charged particle (N)
k_{gas}	Gas correction factor $= \frac{1}{\rho c_p}$ (m^3 K J^{-1})

Kn	Knudsen number $= \dfrac{2\lambda}{d_p}$
l	ESP collector plate length (m)
L	Length of DMA column = 0.444 (m)
m	Particle mass (kg)
M_{Dg0}	Zeroeth moment of Ω in $\widetilde{D}_p$ space
N	Number of measurements
n	Particle number concentration, $dN/dlogd_p$ (# cm^{-3})
P	Duct perimeter (m)
q	Number of elementary charges on particle
Q	Volumetric flow rate inside ESP ($\mathrm{m}^3\ \mathrm{s}^{-1}$)
Q_{mono}	Monodisperse aerosol volumetric flow rate ($\mathrm{m}^3\ \mathrm{s}^{-1}$)
Q_{poly}	Polydisperse aerosol volumetric flow rate ($\mathrm{m}^3\ \mathrm{s}^{-1}$)
Q_{sh}	Sheath volumetric flow rate ($\mathrm{m}^3\ \mathrm{s}^{-1}$)
Q_{tot}	Total volumetric flow rate inside DMA ($\mathrm{m}^3\ \mathrm{s}^{-1}$)
r_1	Inner radius of DMA annulus = 0.937×10^{-2} (m)
r_2	Outer radius of DMA annulus = 1.958×10^{-2} (m)
R^2	Coefficient of determination
Re	Reynolds number $= \dfrac{QD_H}{\nu A}$
$S_{\min}$	Weighted sum of squares

u	Measurement error
v_x	Velocity in x - direction (m s^{-1})
V	DMA rod voltage (V)
w	ESP cavity width (m)
x_0	Initial horizontal coordinate of particle (m)
$x(t)$	Horizontal coordinate of particle position at time t (m)
y_0	Initial vertical coordinate of particle (m)
$y(t)$	Vertical coordinate of particle position at time t (m)
Z_p	Electrical mobility (m^2 V^{-1} s^{-1})
$\overline{Z}_p$	Mean electrical mobility (m^2 V^{-1} s^{-1})
ΔZ_p	Electrical mobility width (m^2 V^{-1} s^{-1})

Greek

λ	Molecular mean free path (m)
μ	Viscosity (N s m^{-2}, Pa s)
ν	Kinematic viscosity (m^2 s^{-1}), degrees of freedom
ρ	Gas density (kg m^{-3})
σ	Standard deviation
σ_{Dg}	Geometric standard deviation of Ω in $\widetilde{D}_p$ space
χ^2	Chi-squared value
Ω	Lognormal transfer function

Acronyms

AIM	Aerosol Instrument Manager®
DMA	differential mobility analyzer
DMM	digital multimeter
ESP	electrostatic precipitator
GIF	Generation IV International Forum
HTGR	high-temperature gas-cooled reactor
NSEI	Nuclear Science and Engineering Institute
PSRC	Particulate Systems Research Center
SMPS	Scanning Mobility Particle Sizer®
TDMA	tandem differential mobility analyzer
UCPC	Ultrafine Condensation Particle Counter®
VHTR	very high temperature reactor

Introduction

Very High Temperature Reactors

The Generation IV International Forum (GIF) made up of 10 countries including the United States has identified the Very High Temperature Reactor (VHTR) as one of six nuclear reactor designs to meet future goals of the nuclear industry. These goals ensure that future nuclear reactor designs provide sustainable energy to both industrialized and developing countries, are economical, incorporate high levels of safety and reliability, and include proliferation resistance and physical protection against acts of terrorism. Furthermore, the GIF hopes to have these designs ready for international deployment before the year 2030 when many of the existing nuclear reactors will be at or near the end of their operating licenses (U.S. DOE, 2002)

VHTRs are graphite moderated, helium cooled, and follow from work completed since the 1960's on high-temperature gas-cooled reactors (HTGRs) including Dragon (Everett, Kinsey & Römberg, 1966), Peach Bottom (Kingrey, 2003), AVR (Cleveland, 1985; Krüger & Ivens, 1985), THTR (Roellig, 1990; Dietrich, Neumann & Roehl, 1997), and Fort St. Vrain (Fuller, 1988) reactors. The VHTR is attractive because of the capability to achieve operating temperatures up to 1000°C and therefore generate electricity using gas turbines with high efficiency (>50%). The high operating temperatures would also allow the VHTR to be used for hydrogen production with high efficiency using thermochemical processes with or without co-generation of electricity (U.S. DOE, 2002; Ghosh & Prelas, 2009).

There are two popular reactor core designs for VHTRs, namely the pebble bed and the prismatic block. Both designs utilize tristructural isotropic (TRISO) fuel particles which are approximately 1 mm in diameter and contain a fissile kernel (i.e. UO_2, UC_2) surrounded by four protective coatings designed to contain fission products and gases while providing thermal and structural support. Figure 1 below shows a schematic of a typical TRISO fuel particle with the fuel kernel and the surrounding layers. Other fissile fuels such as spent light water reactor fuel, weapons surplus Pu, or Th may also be used which extend the capabilities of the TRISO fuel particle and help to reduce nuclear waste and proliferation (Venneri, 2005).

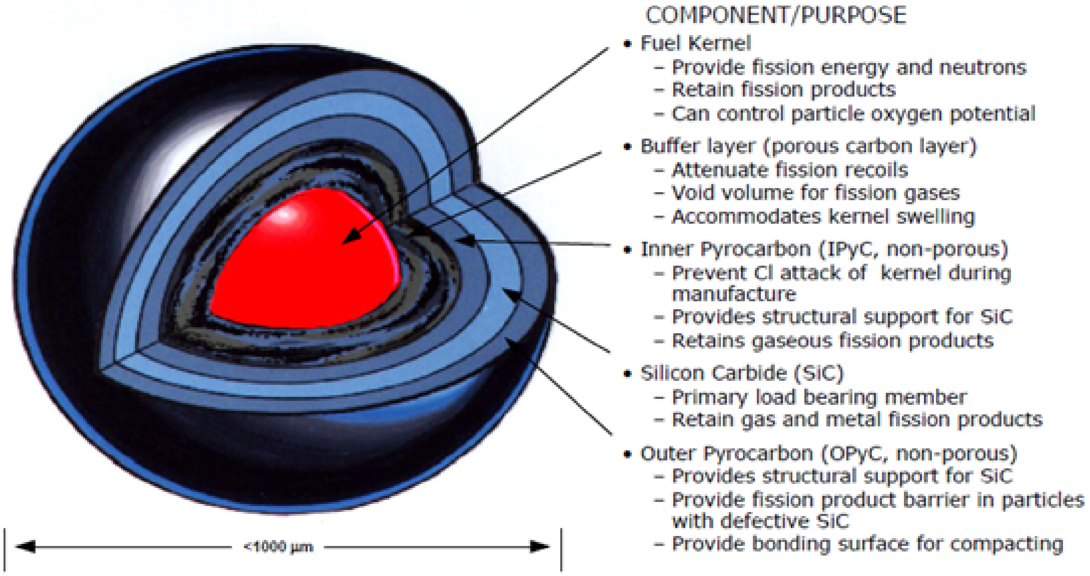

Figure 1. TRISO fuel particle (Venneri, 2005).

For the pebble bed design, the TRISO fuel particles are mixed with graphite powder and pressed into spheres or "pebbles" that are approximately 60 mm in diameter (as shown in Figure 2a). On the order of 360,000 pebbles, each containing approximately 11,000 TRISO fuel particles, are circulated through a reaction chamber where the nuclear fuel is inserted at the top, consumed as they settle toward the bottom, and subsequently removed from the reactor (Kadak, 2005). Furthermore, the pebbles can be examined upon exiting the reaction chamber, checked for fuel consumption and defects, and recirculated as necessary to minimize waste. In contrast, for the prismatic block design the TRISO fuel is mixed with graphite powder and pressed into a cylinder which is placed into a stationary arrangement within the reactor core (shown in Figure 2b). The main advantage of the pebble bed reactor is online refueling while the prismatic block design, like traditional nuclear reactor designs, requires the reactor to be shut down during refueling. Both reactors have promise as modular designs which would allow for variable plant capacity by subsequent addition of modules, as well as reduce cost by subassembly in a factory setting and reduction in the payback period by bringing the modules online as they are constructed.

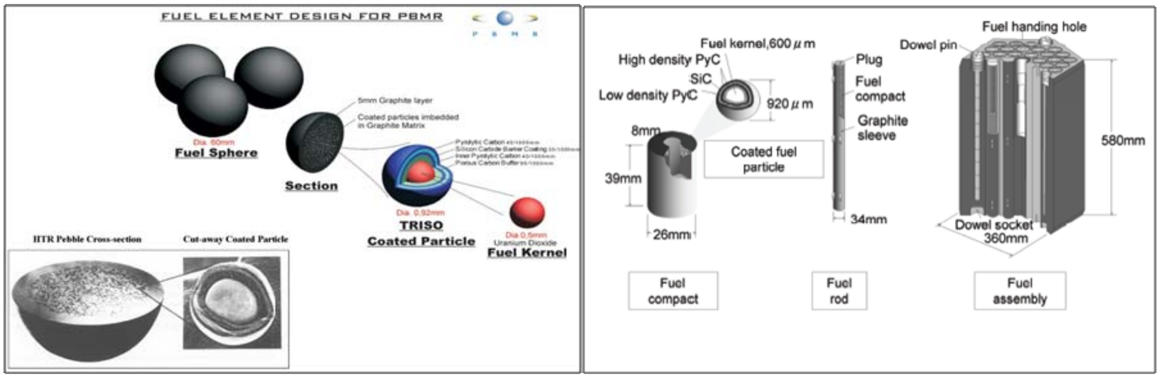

(a) (b)

Figure 2. (a) Pebble for PBR (PBMR, 2010) (b) prismatic block fuel assembly (Takamatsu et al., 2006).

Fission Product Release

TRISO fuel particles are designed to retain fission products and gases throughout their lifetime although some amount of fission product release is inevitable due to limitations in manufacturability, in service failures, and the performance of TRISO coatings toward certain isotopes. Manufacturing defects leading to fission product release from TRISO fuel particles include cracked coatings and uranium contamination in the graphite. Manufacturing defects in the TRISO coatings may lead to cracking and failure of the SiC and/or PyC layers during service. Failures which expose the kernel will release fission gases, while failure of any layer will release fission metals (Wichner, 1991). To minimize failure and uranium contamination of the graphite the TRISO particles are manufactured with low defect fractions. The defect fractions account for the free uranium either introduced from uranium contamination or from particles with cracked or permeable layers. Tables 1 & 2 give the U.S. TRISO as-fabricated fuel quality and end-of-life fuel performance specifications (IAEA, 1997), respectively. End-of-life specifications under normal operating conditions require a defect fraction $\leq 4.0\times10^{-4}$ at 95% confidence interval, amounting to approximately four defective particles per fuel element. In general the SiC and PyC layers are designed to withstand the harsh environment within the containment vessel while retaining fission products produced in the kernel. These layers are efficient at retaining most fission products although Ag in particular has been shown to diffuse through the SiC layer of intact particles (Wichner, 1991).

Aerosol Generation in VHTRs

One of the design challenges of the VHTR is the production of aerosols during normal operation and in the event of an accident. Pebble bed reactors create graphite dust due to mechanical abrasion among pebbles as they flow through the reactor core and throughout the distribution circuits. Inside the reactor core, the dust is lifted by the helium coolant creating graphite aerosol which is carried throughout the cooling circuit and possibly into the gas turbine. Various fission products also constitute a fraction of the aerosol within the reactor due to failed (i.e. cracked or broken) fuel particles and diffusion through TRISO coatings. Dust accumulation can damage system components such as the gas turbine and also become a health hazard for personnel during plant maintenance (Moormann, 2008). Furthermore, several accident scenarios such as air ingress (IAEA, 1997), water ingress (IAEA, 1997; Kugeler, Stulgies, & Epping, 1988), and depressurization (IAEA, 1997; Stempniewicz, Komen, & de With, 2008; Wichner, 1991) may lead to the generation and release of aerosol and fission products from both pebble bed and prismatic block reactors. It is therefore important to characterize and understand the behavior of aerosols generated within these reactors to improve their design and properly assess accident scenarios.

Table 1

As-Fabricated Quality Requirements for NP-MHTGR Fuel (IAEA, 1997, p. 40)

Quality requirements	**Fraction fissile or fertile**	
	Mean	**95% confidence < 5% compacts exceed**
Fuel Particles		
Defective SiC	$\leq 5.0\times10^{-5}$	$\leq 1.0\times10^{-4}$
Total heavy metal (HM) Contamination	$\leq 1.0\times10^{-5}$	$\leq 2.0\times10^{-5}$
Total fraction HM outside intact SiC	$\leq 6.0\times10^{-5}$	$\leq 1.2\times10^{-4}$
Missing or defective buffer	$\leq 5.0\times10^{-5}$	$\leq 2.0\times10^{-5}$
Missing or defective inner PyC	$\leq 4.0\times10^{-5}$	$\leq 1.0\times10^{-5}$
Missing or defective outer PyC	$\leq 1.0\times10^{-4}$	$\leq 1.0\times10^{-3}$
Fuel compacts		
Defective SiC	$\leq 5.0\times10^{-5}$	$\leq 1.0\times10^{-4}$
Uranium contamination	$\leq 1.0\times10^{-5}$	$\leq 2.0\times10^{-5}$
Total fraction HM outside intact SiC	$\leq 6.0\times10^{-5}$	$\leq 1.2\times10^{-4}$
Missing or defective inner PyC	$\leq 4.0\times10^{-5}$	$\leq 1.0\times10^{-4}$

Table 2

NP-MHTGR End-of-Life Fuel Performance (IAEA, 1997, p. 40)

Parameter	**NP-MHTGR driver fuel Allowable fraction (core average)**	
	> 50% confidence	**> 95% confidence**
Fuel failure during normal operation	$\leq 1.0\times10^{-4}$	$\leq 4.0\times10^{-4}$
Incremental failure during design basis accident	$\leq 3.0\times10^{-4}$	$\leq 1.2\times10^{-3}$

Aerosol Characterization

The dry environment within gas cooled reactors introduces new design issues associated with aerosol coagulation and deposition, as stated in a recent report by the Nuclear Regulatory Commission (NRC):

> Certainly in the containment and to some extent in the reactor coolant system, radionuclide transport will be predominantly by aerosol transport. Modeling of conventional aerosol has been well developed and validated by the NRC, and routine calculations can be done. By and large these computational tools have been optimized for rather "wet" or highly humid environments. The dry environment typical of many classes of gas reactors will pose a challenge. In such dry environments, water condensation within the interstices of particle agglomerates will not be possible. There will, then, not be a strong surface tension driving force to convert linear-chain agglomerates into more spherical aerosol particles assumed for the analyses with existing computer codes. Shape factors will have to be introduced into the calculations, and these shape factors will not necessarily be small. Kops and coworkers have reported shape factors as high as 35 for dry aerosols formed from the condensation of high-temperature vapors.

> Furthermore, the shape factors will vary with particle size—something codes such as MAEROS, used widely for nuclear application, cannot handle.
>
> A more bothersome issue is that of electrostatic charging of aerosols in the dry environment. Aerosol particles can be charged in the dry environment because of gas-phase ions formed in the intense radiation field. Negatively charged ions typically have higher mobilities than do positively charged ions. Consequently aerosol particles are bombarded more often by negatively charged ions and can assume a negative charge. The magnitude of the charge depends on the particle size. Coulombic forces among aerosol particles due to like charges on particles are not addressed in currently available models of aerosol behavior. The electrostatic forces among charged particles are much stronger than the forces that ordinarily drive the agglomeration of aerosol particles to sizes such that they readily deposit by gravitational settling or inertial impaction on structures. What deposition of particles does occur will develop either a surface charge or a mirror image charge that could also produce forces capable of interfering with the deposition of additional particles. Again, current models do not account for such effects that are important only where the radiation field is large. (Morris, 2008, pp. A2–A3)

As described above particle charge will play an important role on the behavior of aerosols within gas cooled reactors such as the VHTR. These aerosols can become charged due to ionizing radiation within the environment as previously mentioned and also from radioactive decay by emission of charged particles (i.e. α^{2+}, $\beta^{\pm}$) from fission products resulting in “self-charging” of aerosol particles (Gensdarmes, Boulaud, & Renoux, 2001).

Radioactive aerosols have been investigated theoretically and models have been developed for the charge distribution in both monodisperse (Clement & Harrison, 1992) and polydisperse (Clement, Clement, & Harrison, 1995) aerosols. Clement and Harrison (1992) have examined the charging process and charging rate of radioactive aerosols, and have presented equations for the charge distributions and ion concentrations of radioactive aerosols. They have compared their theoretical models to previous experimental results for monodisperse aerosols including ^{198}Au (Yeh, Newton, Raabe, & Boor, 1976) and $^{238}PuO_2$ (Yeh, Newton, & Teague, 1978) and found good agreement. Clement, Clement, and Harrison (1995) have extended the theory to account for charging of polydisperse radioactive aerosol and have calculated the charge distributions of both a Cs aerosol at normal temperatures and a highly radioactive aerosol containing ^{131}I within a containment atmosphere. Both calculations show positive charging at large sizes and negative mean charges at small sizes. Calculations were also performed on the effects of radioactive aerosol charging on Brownian coagulation rates between a small radioactive aerosol and a larger-sized passive aerosol, and also for an α-decaying aerosol. The results indicate that the presence of radioactive aerosols can greatly enhance coagulation rates and will be an important factor in future models for predicting the transport and behavior of radioactive aerosols. Clement and Harrison (2000) have also investigated the enhancement of self-charging of radioactive aerosols by the reduction of ions in the surrounding gas. The presence of ions in the surrounding gas partially neutralizes the aerosol by ion attachment, however, the neutralizing effect can be reduced by reducing the ion concentration either by diluting the aerosol, using a confined geometry, or removal by electric fields. Enhancement in a confined geometry occurs when the energy of the ionizing radiation is mainly deposited in the surrounding container instead of the surrounding gas and is particularly important for β-particles which have longer ranges than α-particles.

Experimental investigations of the charge distributions of radioactive aerosols have been limited to monodisperse aerosols due to the limitation in experimental techniques. Gensdarmes et al. (2001) used a radial flow differential mobility analyzer with a condensation nucleus counter to obtain the charge distribution of aerosol droplets produced using a vibrating orifice aerosol generator containing a solution of ^{137}Cs, hydrochloric acid, and cesium chloride. The results were compared with the theory developed by Clement and Harrison (1992) and were in good agreement. Another study by Emets, Kasheev, and Poluektov (1991) measured the charge distributions of polydisperse aerosols using a differential mobility analyzer in series with an aerosol size analyzer. However, this method was restricted to particles in the diameter range of 0.3–10μm because the aerosol size analyzer measures particle size based on light scattering intensity. Both of these experiments involved aerosols that are not expected within the VHTR reactor and therefore more realistic measurements are necessary. Yeh et al. (1976) measured the self-charging effects of two different sized ^{198}Au-labeled monodisperse gold aerosols using an aerosol electrical mobility spectrometer and found that the charge distributions show a shift to a net positive charge and therefore deviate from Boltzmann equilibrium. The shift was found to be dependent on the specific activity of the aerosol and showed increased positive charges with increasing specific activity. Yeh et al. (1978) extended this work by examining the equilibrium charge distributions of monodisperse $^{238}PuO_2$ and polydispersed plutonium mixed oxide aerosols using a parallel plate miniature aerosol electrical mobility spectrometer. The sample aerosols were first neutralized using a ^{85}Kr discharger before entering the spectrometer and the degree of self-charging was determined by the deviation of the measured charge distribution from the Boltzmann charge distribution. The results showed a slight positive shift from the Boltzmann charge distribution with an estimated charging time of 30–120 seconds.

To quantify the charge effects of aerosols within VHTRs, it is necessary to experimentally determine their charge distributions. Currently no such studies have been reported, most likely due to the lack of experimental techniques and difficulty in working with radioactive aerosols because of their complexity and safety issues (Gensdarmes et al., 2001). Closely related work includes the formation of graphite aerosol during water ingress into the core of a pebble bed reactor (Kugeler, Stulgies, & Epping, 1988), carbon and fission product plateout and liftoff models in the HTGR primary circuit (Wichner, 1991), carbon transport in HTGRs (Everett, Kinsey, & Römberg, 1966), and resuspension of radioactive graphite dust within HTGR reactors (Stempniewicz, Komen, & de With, 2008), although none of these studies consider the charge distributions of such particles.

Until recently only techniques for measuring the charge distribution of monodisperse and large (>0.3 μm) polydisperse aerosols have been available. In 2005, Kim, Woo, Liu, and Zachariah described a technique for measuring the size and charge distributions of nanosized aerosols sampled from a diffusion flame using a tandem differential mobility analyzer (TDMA). Subsequently Maricq released results using the TDMA technique to measure the size and charge distributions of particles in premixed flames (Maricq, 2005, 2006a, 2008a, 2008b), vehicle exhaust (Maricq, 2006b, 2008a, 2008b), and oil droplets (Maricq, 2008a). These studies have shown the applicability of the TDMA method toward the measurement of the size and charge distributions of nanosized aerosols, although the results are not applicable to VHTRs. Furthermore, the data reduction techniques used to obtain the size and charge distributions were either poorly described or relied on additional measurements such as the total particle concentration using a Differential Mobility Particle Sizer (SMPS) and the ion concentration using a Langmuir probe.

Problem Statement

For the design of future VHTR reactors, and also for accurate accident modeling, the knowledge of the charge distribution among graphite and fission products is very important. Currently no work has been reported on the charge distribution of these aerosols. The present research is concerned with the investigation of using a TDMA toward the measurement of these aerosols. This work will specifically examine how the TDMA method performs in measuring the charge distributions among graphite, palladium, and silver aerosols generated by an electric discharge technique. In addition, since the measurement technique is independent of particle generation, successful measurement of the charge distribution of these types of aerosols using the TDMA method will warrant further investigation toward the application of the TDMA method in measuring radioactive graphite and associated fission products present within VHTRs. Gold aerosols will also be characterized due the interest and broad application of gold nanoparticles in the biomedical field. Furthermore, since the spark generator is commonly used in various areas of scientific research, such as combustion emissions research, knowledge of the charge distribution of graphite aerosol created by the electric discharge technique is also of interest.

Objectives

Several objectives will be pursued over the duration of the project. These include:

1. To build and calibrate a working tandem differential mobility analyzer (TDMA) using a TSI® 3071A Electrostatic Classifier, a TSI® 3080 Electrostatic Classifier, and a TSI® 3776 Ultrafine Condensation Particle Counter (UCPC).
2. To design, construct, and test an electrostatic precipitator for neutral particle measurement using the TDMA apparatus.
3. Use the constructed TDMA apparatus to measure the size and electrical mobility distributions of graphite, palladium, silver, and gold aerosols generated using a PALAS® GFG-1000 spark generator for positive, negative, and neutral particle polarities.
4. Analyze the acquired data using a Mathematica® algorithm developed by Simones, Gutti, Meyer, and Loyalka (2011) at the University of Missouri to obtain the size and charge distributions of the measured aerosols.

The equipment listed within the objectives is located at the Nuclear Science and Engineering Institute's (NSEI) Particulate Systems Research Center (PSRC) at the University of Missouri where this work will be carried out. Furthermore, this project will establish both knowledge and a working TDMA apparatus for future fission product transport research at NSEI.

Method

Apparatus

Multiple instruments were used in this study including a PALAS® GFG-1000 spark generator, a TSI® 3071A Electrostatic Classifier, A TSI® 3936 Scanning Mobility Particle Sizer (SMPS) spectrometer, and an electrostatic precipitator (ESP) designed and built in-house as shown in Figure 3. The TSI instruments together constitute the tandem differential mobility analyzer (TDMA) used as the principle apparatus in this study. The exact instrument configuration will be discussed in this section along with the function and operation of each instrument listed above.

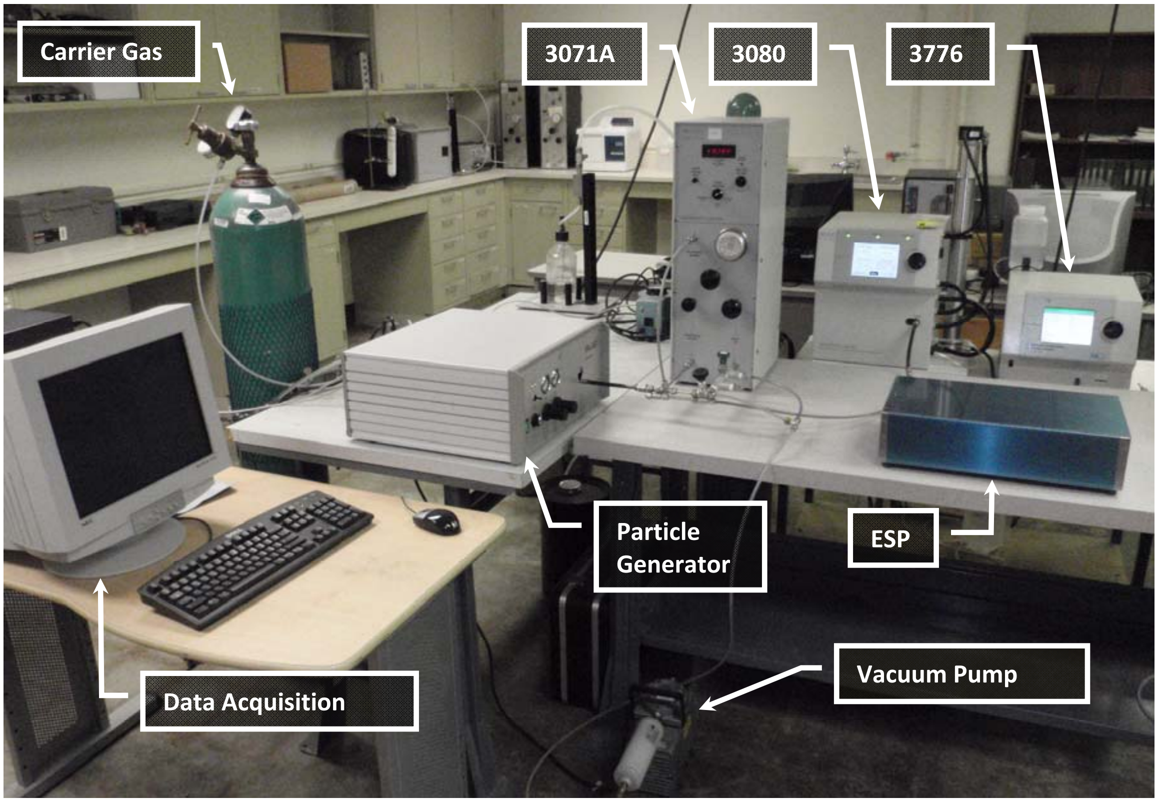

Figure 3. Experimental setup for charged particle size and charge distribution measurement. Components of the setup are labeled.

PALAS GFG-1000 Spark Generator

The spark generator produces carbon nanoparticles through an electric spark discharge process across two graphite electrodes positioned end-to-end within a gas chamber as shown in Figure 4. An inert carrier gas, such as argon or N_2, is directed between the electrode gap to transport the evaporated carbon away from the electrodes where it then condenses to form nanoparticles. The suspended particles form a primary aerosol which will further coalesce and coagulate increasing the average particle size. Average particle size can be manipulated by user defined parameters such as the carrier gas flow rate and spark frequency which adjust the particle concentration and therefore the coagulation rate. Although this device is primarily designed for graphite, custom electrodes have also been constructed for the production of palladium, silver, and gold aerosols. Figure 5 shows transmission electron micrographs of the generated particles. Gold, palladium and silver show simple, nearly spherical structure while the graphite particles are complex chain agglomerates.

TSI 3071A Electrostatic Classifier

The TSI model 3071A Electrostatic Classifier includes an aerosol charge neutralizer, differential mobility analyzer (DMA), associated electronics, and an instrument panel for voltage and flow rate adjustments. The charge neutralizer shown in Figure 6a contains a ^{85}Kr radioactive source of β^- particles (i.e. electrons) creating a high concentration of bipolar ions within the neutralizer cavity. As the aerosol flows through the cavity the particles collide with charged ions and reach a bipolar charge equilibrium which has been described theoretically by Fuchs (1963) and validated experimentally by Wiedensohler (1986). During operation, the aerosol first enters the charge neutralizer

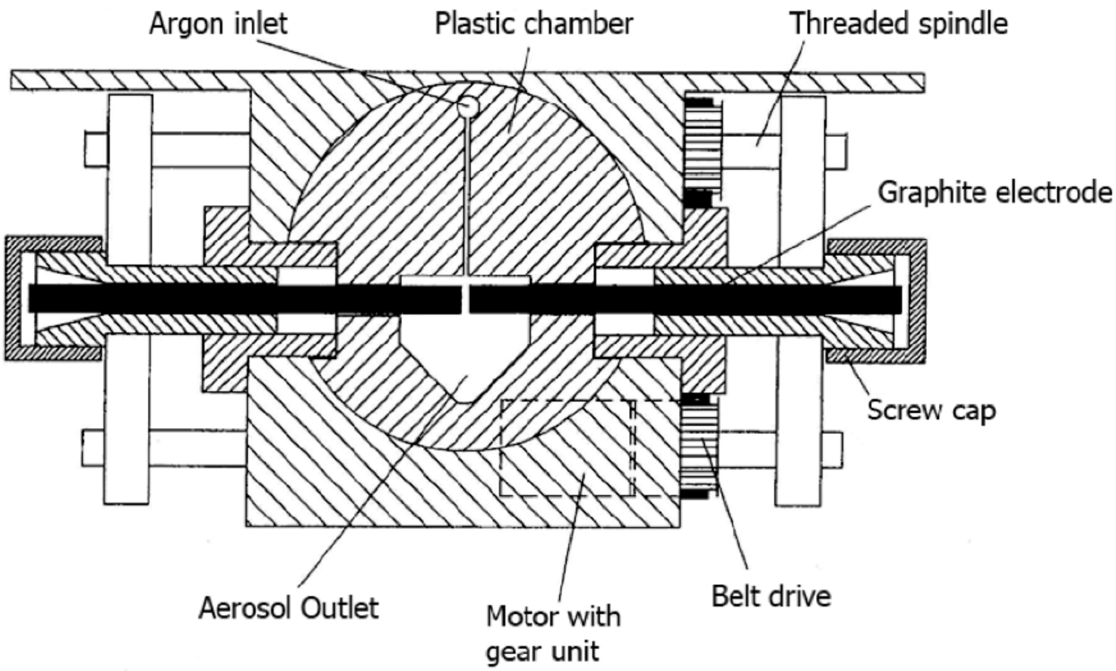

Figure 4. Cross section of spark generator electrode unit (adapted with permission from PALAS, 2003).

before entering the DMA so that the aerosol charge becomes a known quantity and the DMA can be used for particle size measurements. The main purpose of the DMA is to allow the selection of aerosol particles with the same electrical mobility, although it can also be used for measuring the charge of a monodisperse aerosol of known size or for measuring the size distribution of a polydisperse aerosol when the charge distribution is known. The DMA consists of an annulus made up of a stainless steel tube and electrode, or high voltage rod, as shown in Figure 6b. A sheath gas, typically air, is introduced at the top of the column and is used to shield the electrode from random interaction with aerosol particles. The aerosol is introduced around the outer perimeter of the annulus and flows down the side of the tube alongside the sheath air. A voltage is applied between the center electrode and the tube wall creating an electric field in the annular region. Within

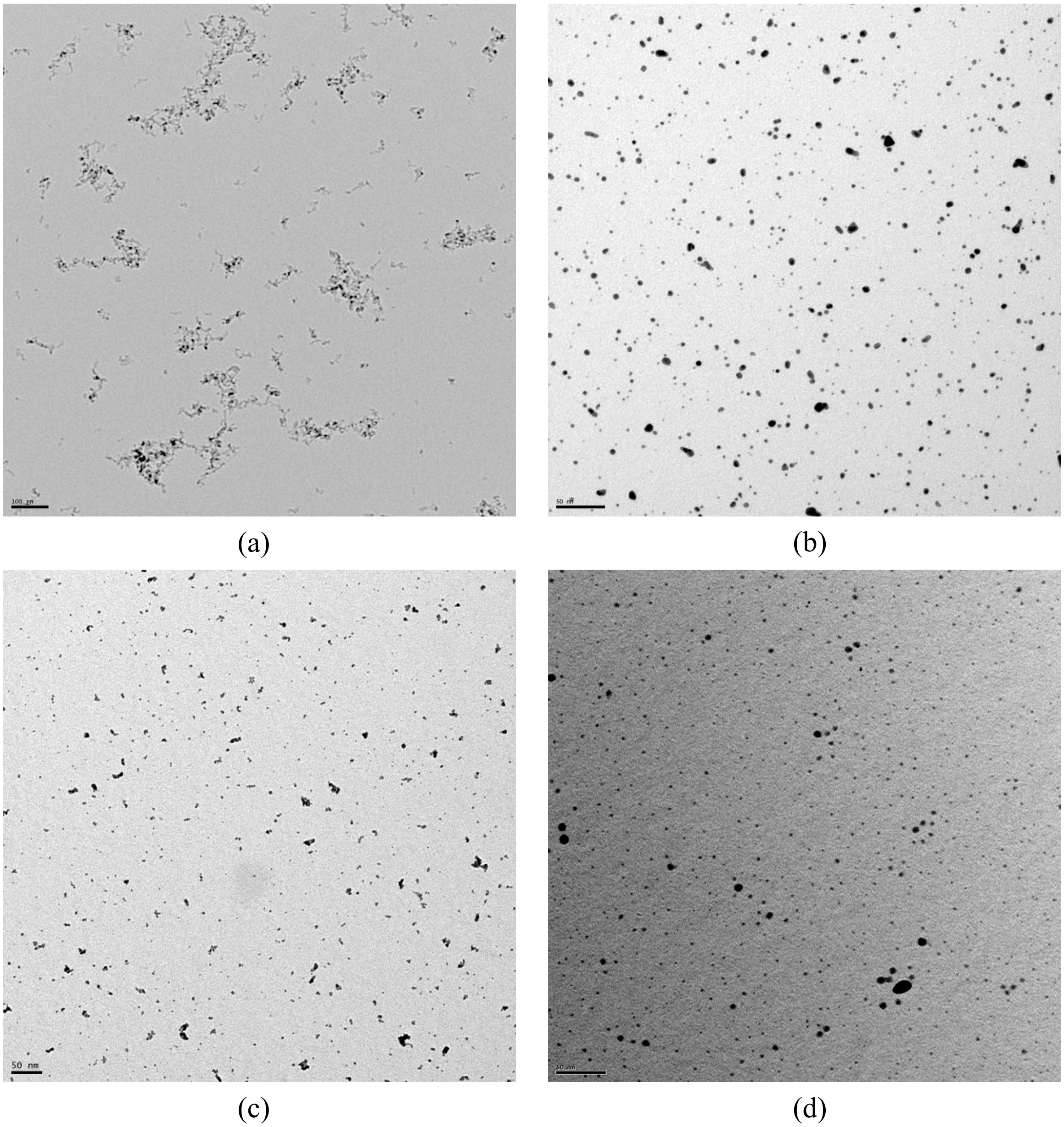

(a) (b)

(c) (d)

Figure 5. Transmission electron micrographs of spark generated (a) graphite (100 µm), (b) gold (50 µm), (c) palladium (50 µm), and (d) silver (50 µm) nanoparticles (courtesy of Dr. Veera Rajesh Gutti, NSEI).

the electric field neutrally charged particles simply follow the streamlines of the flow, while charged particles are, in addition, attracted toward the center electrode causing them to penetrate the sheath flow resulting in curved trajectories dictated by their electrical mobility. A small sampling slit near the bottom of the electrode acts as a filter which separates particles that fall in this region from the main flow. The voltage applied to the center electrode, either positive or negative, is varied to change the particle trajectories within the annulus and thereby controls the particle mobility that enters the sampling slit. The remaining particles exit the DMA with the excess gas where they are filtered and pulled through a vacuum pump which provides the pressure difference to drive the sheath flow.

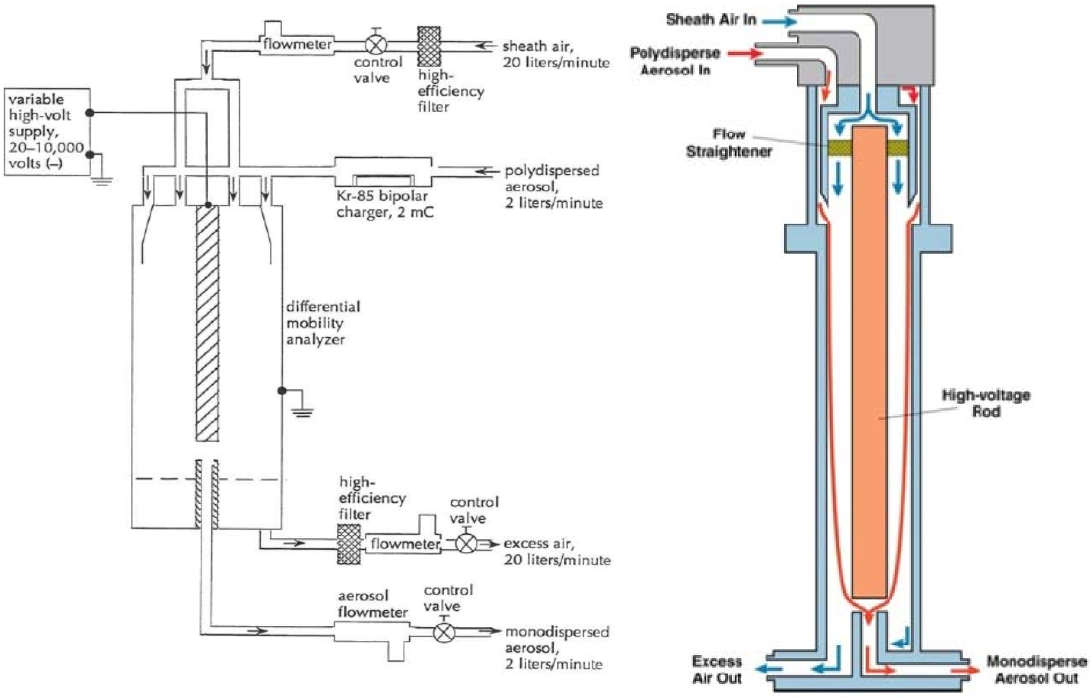

(a) (b)

Figure 6. (a) Schematic showing main components of TSI 3071A Electrostatic Classifier (Adapted with permission from TSI, 1994) (b) Schematic of typical DMA column showing gas flow paths and charged particle trajectories (adapted with permission from TSI, 2008).

Due to the finite width of the sampling slit there will be a small range of electrical mobilities which pass through. The mean electrical mobility ($\overline{Z}_p$) and mobility width (ΔZ_p) entering the sampling slit are functions of the DMA geometry, aerosol and sheath flow rates, and the rod voltage as given below (Knutson, 1971),

$$\overline{Z}_p = \frac{\left[Q_{tot} - \frac{1}{2}\left(Q_{mono} + Q_{poly}\right)\right]}{2\pi VL}\ln\left(r_2 / r_1\right) = \frac{Q_{sh}}{2\pi VL}\ln\left(r_2 / r_1\right)\Bigg|_{Q_{mono}=Q_{poly}} \tag{1}$$

$$\Delta Z_p = \frac{\left(Q_{mono} + Q_{poly}\right)\ln\left(r_2 / r_1\right)}{2\pi VL} \tag{2}$$

Here it follows from continuity that $Q_{tot} = Q_{sh} + Q_{poly}$ assuming incompressible flow. Knutson (1971) also derived an expression for the appropriate rod voltages to use such that the edges of consecutive electrical mobility regions align,

$$R = 1 - \frac{Q_{mono} + Q_{poly}}{Q_{tot}} \tag{3}$$

$$V_{i+1} = R^i \cdot V_1 \quad i = 1, 2, 3, \ldots \tag{4}$$

After selecting a starting voltage (V_1) all consecutive voltages can be determined to measure the entire electrical mobility range. The original factory DC-HV DC converter installed in the TSI 3071A was designed to maintain a negative potential on the DMA center electrode (0 to -10,000 V) for sampling positively charged particles and allowed for only single polarity measurements. To measure bipolar charge distributions this has been replaced with a commercially available DC-HV DC converter with dual polarity outputs (EMCO F121CT) providing positive and negative voltage ranges of 0 to 7,000 V and 0 to -7,000 V, respectively.

TSI 3936 Scanning Mobility Particle Sizer (SMPS)

The SMPS is made up of two principle instruments namely an electrostatic classifier and a condensation particle counter. The configuration used in this study included a TSI 3080 Electrostatic Classifier and a TSI 3776 Ultrafine Condensation Particle Counter (UCPC). The TSI 3080 Electrostatic Classifier is an updated version of the TSI 3071A that includes a digital interface and integral compressors for the sheath flow rate as shown in Figure 7. Using built-in digital flow meters, the instrument automatically regulates the user defined sheath flow rate which is recirculated from the main outlet of the DMA. Gas recirculation creates a partially closed system with a single inlet and outlet for the polydisperse and monodisperse aerosol, respectively.

As particles are selected out based on their size they are directed to the UCPC where the particles are counted to obtain the size distribution. The UCPC works by first dividing the aerosol flow into two parts. The first part is filtered and passed by a butyl alcohol-saturated wick where the alcohol is evaporated into the gas stream. The second part is sent through a capillary tube and into a condenser where it combines with the first stream and cooled. As the temperature of the mixture decreases the saturation ratio of the alcohol increases and subsequently causes heterogeneous nucleation promoted by the presence of the aerosol particles. The enlarged particles then enter a laser cavity where they can then be optically detected by using a photodiode to sense scattered laser light. A flow diagram of the UCPC is shown below in Figure 8.

The DMA rod voltages of the SMPS are controlled using the TSI Aerosol Instrument Manager (AIM) software package. During measurement the DMA rod voltage is swept continuously allowing for quick measurement of the particle size distribution.

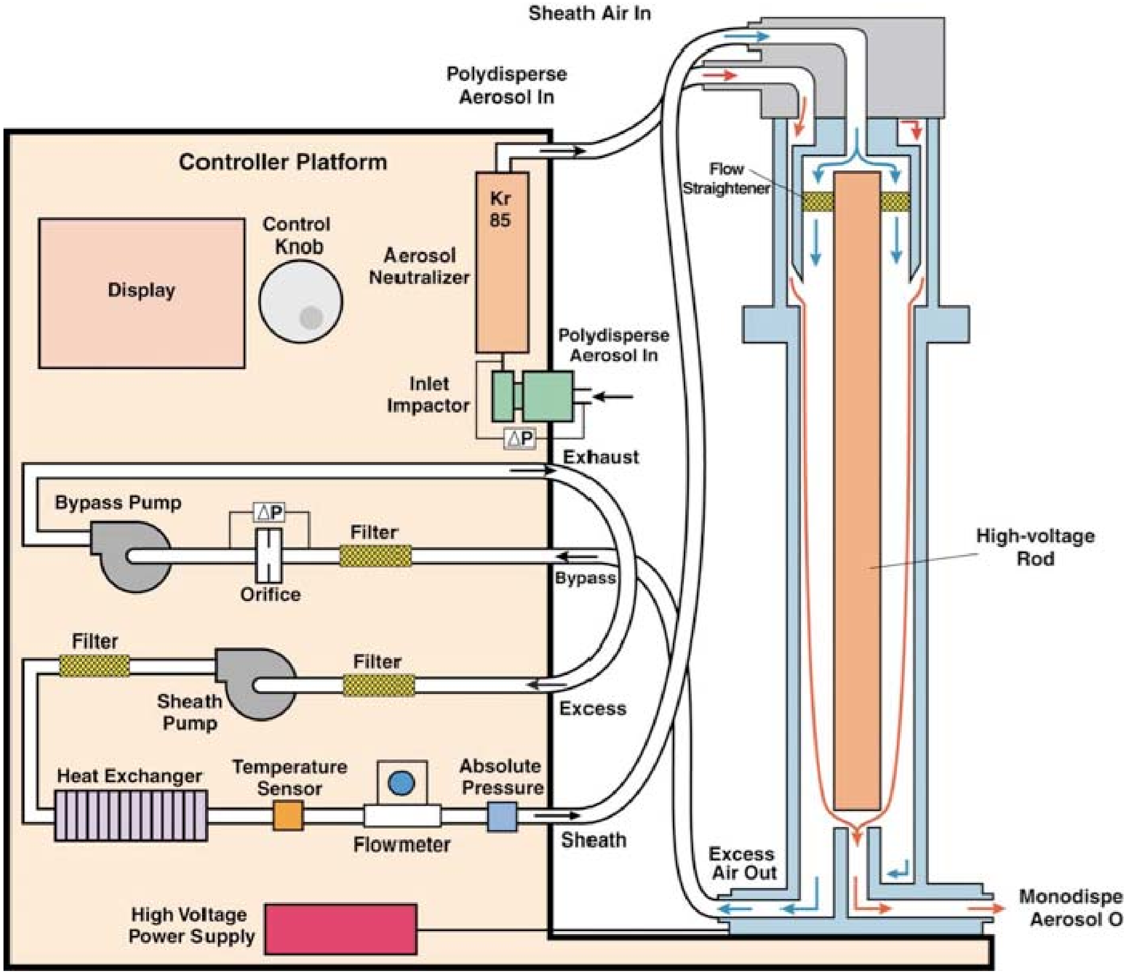

Figure 7. Schematic of the TSI 3080 Electrostatic Classifier (adapted with permission from TSI, 2008).

The software communicates directly with the UCPC which then controls the rod voltage applied to the 3080 classifier. The AIM software uses input parameters such as sheath and aerosol flow rates, gas properties such as viscosity and mean free path, and voltage polarity. During measurement the software package takes raw count data and can calculate size distributions weighted by number, diameter, surface area, volume, or mass. Various statistics such as concentration, mode, median, mean, geometric mean, and geometric standard deviation are also calculated for number, surface area, volume, and mass moments.

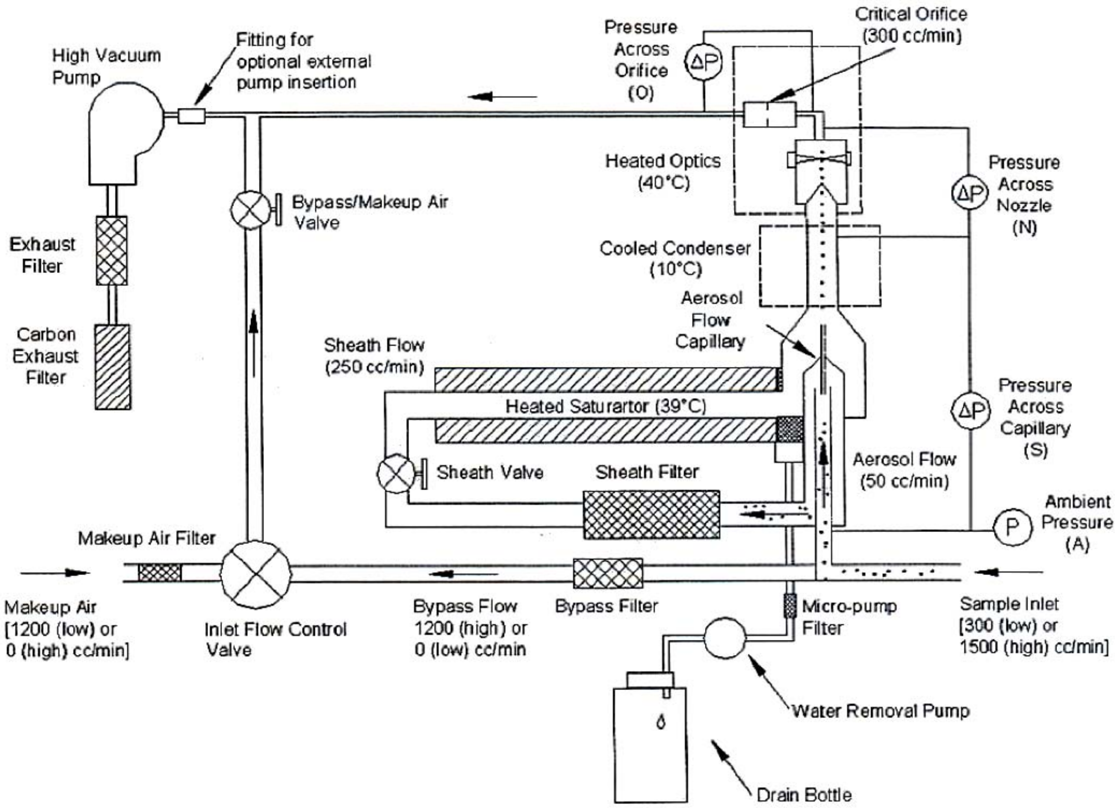

Figure 8. Schematic of the TSI 3776 Ultrafine Condensation Particle Counter (adapted with permission from TSI, 2007).

Tandem Differential Mobility Analyzer

The TDMA was assembled by connecting the 3071A classifier in series with the SMPS spectrometer as shown in Figure 9a. This way an aerosol of unknown size and charge can be quantified by first using the 3071A classifier with the charge neutralizer removed to preserve the original aerosol charge and classify particles solely based on their electrical mobility. By fixing the voltage of the first classifier particles of constant electrical mobility (i.e. small singly charged particles and larger multiply charged particles) will be supplied to the 3080 classifier of the SMPS spectrometer where the original charge is first replaced with a bipolar charge distribution using a charge neutralizer before the particle size distribution is measured. The process is repeated for multiple voltages of the 3071A classifier, given by Equations (3) & (4), obtaining particle size distributions as a function of electrical mobility.

Electrostatic Precipitator

To determine the size distribution of the neutrally charged particles exiting the spark generator a parallel plate electrostatic precipitator (ESP) was constructed to remove charged aerosol particles before entering the SMPS for size measurement. The instrument configuration for neutral particle measurement is shown below in Figure 9b and details on the ESP design process can be found in Appendix A.

Instrument Setup and Calibration

3071A digital voltage indicator calibration

Since the DMA rod voltage is a critical parameter in both the mobility measurements and calculations the digital voltage readout on the 3071A classifier was calibrated against a Fluke 87 Digital Multimeter (DMM). To measure voltages above the DMM limit of 1 kV a Fluke 80k-15 Electronic Air Cleaner Probe (subsequently referred to as a high voltage probe) was used to extend the voltage range of the DMM to 15 kV. Measurement of the 3071A DMA rod voltage included ±0.05% accuracy and varying resolution error from the DMM, and ±2% accuracy error from the high voltage probe. The resolution of the DMM changed over the measurement interval between 0–10 kV and varied from 0.01–1 V. Design stage uncertainty was calculated following the root-sum-of-squares (RSS) method (Figliola & Beasley, 2006) as shown in Equation (5).

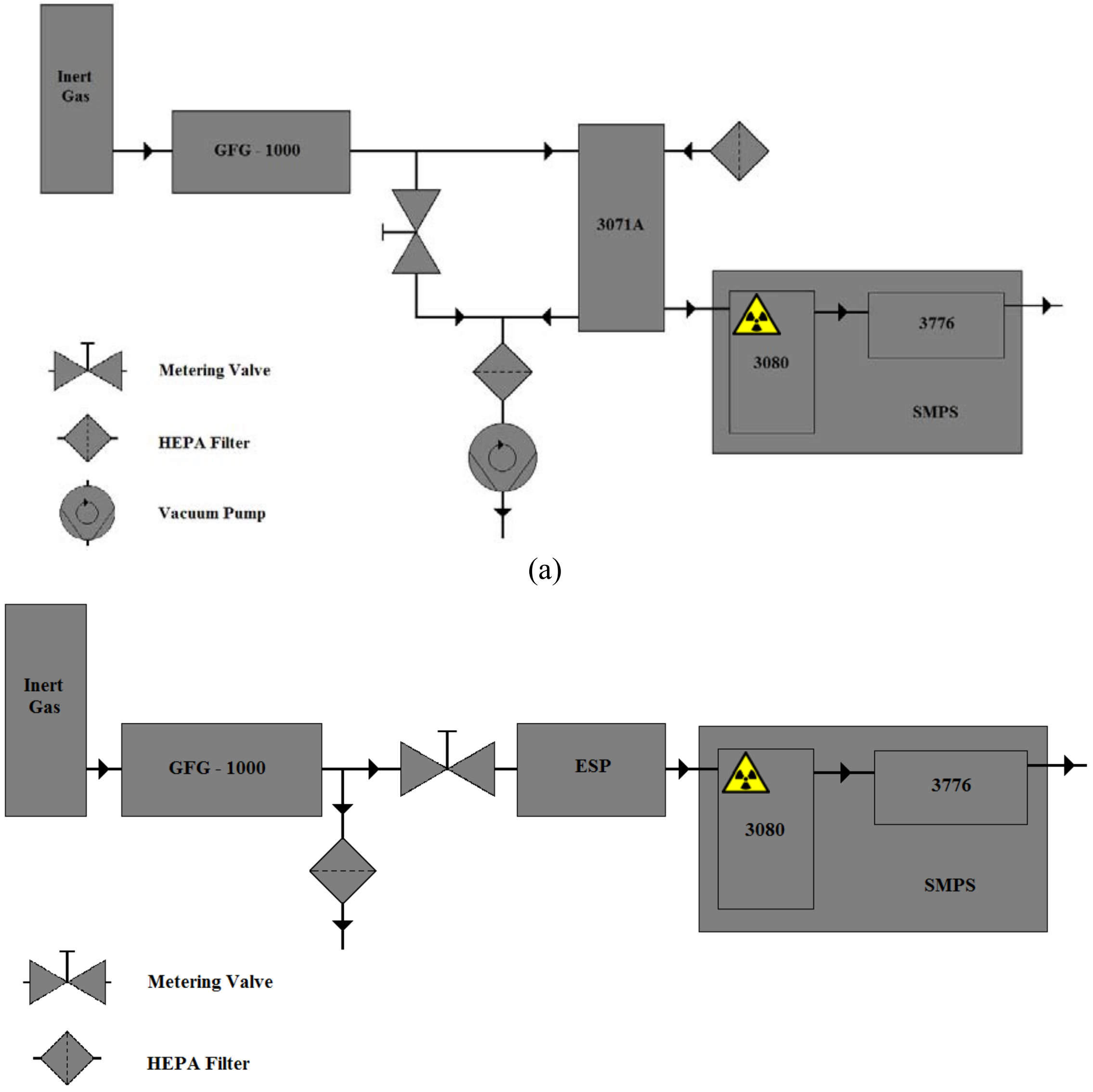

(a)

(b)

Figure 9. Flow diagram of the (a) TDMA apparatus used for charged particle measurement and the (b) ESP apparatus used for neutral particle measurement.

$$u_{V_i} = \sqrt{u_{res,i}^2 + \sum u_j^2} = \sqrt{u_{res,i}^2 + V_i^2\left(0.0005^2 + 0.02^2\right)} \tag{5}$$

Figure 10 below shows the calibration chart obtained with the associated error bars and the results are summarized in Table 3. Linear regression was also used to obtain a least squares fit for both the negative and positive ranges of the calibration curve. Data obtained during voltage calibration can be found in Appendix B and details on the linear regression procedure are given in Appendix D.

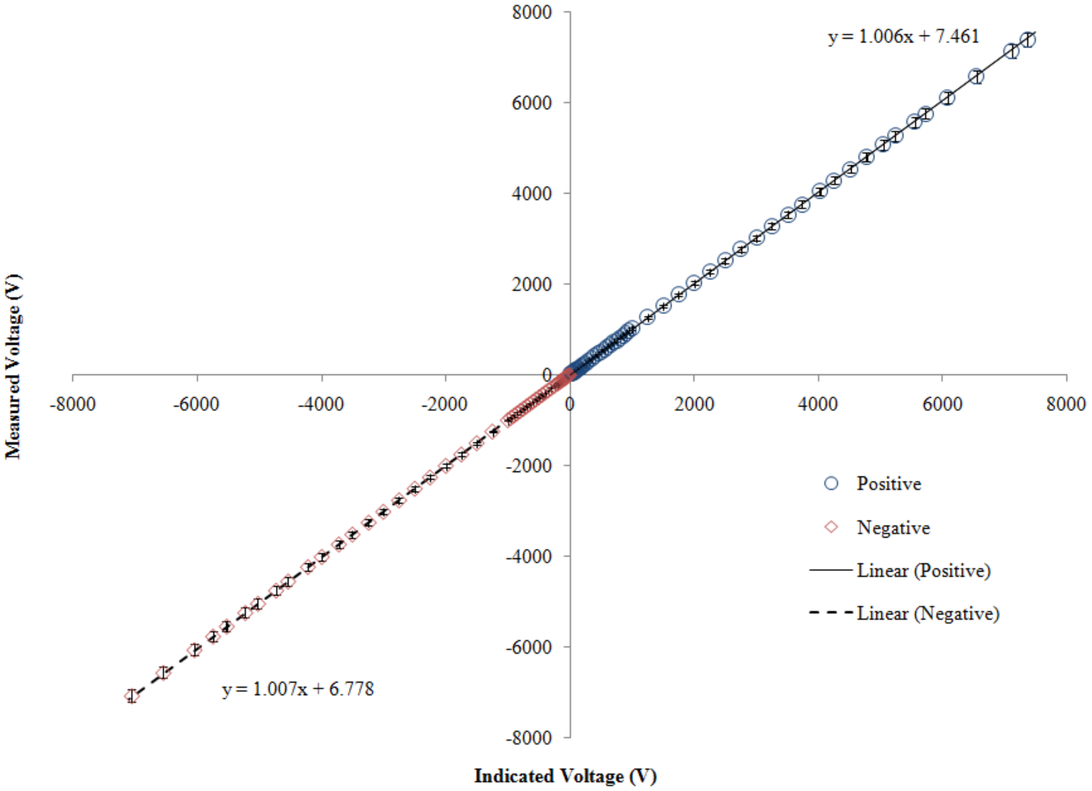

Figure 10. 3071A digital voltage indicator calibration chart.

Table 3

3071A Voltage Indicator Calibration Linear-Least-Squares-Fit Results

Polarity	a (V)	σ_a (V)	b	σ_b	$\delta y_{95\%}$	n	ν	R^2
Positive	7.5	0.3	1.006	0.003	0.04	54	52	1.00
Negative	6.78	0.07	1.007	0.003	0.04	53	51	1.00

3080 indicated sheath flow rate for N_2 gas

When using the ESP the particles and the carrier gas are moved through the ESP and into the 3080 classifier. Since the 3080 classifier built-in electronics are calibrated for air, the indicated sheath flow rate will not be correct when using other gases. These effects are not present when using the TDMA because the 3071A uses air as the sheath gas which becomes the carrier gas for the monodisperse aerosol. The 3080 classifier has a single digital flow meter which the instrument uses to maintain the user sheath flow rate settings. This flow meter was calibrated for N_2 gas by connecting an AALBORG GFM37 Mass Flow Meter in line with the built-in flow meter of the 3080 classifier and comparing the indicated and actual flow rates (see Appendix C for data). Design stage uncertainty for the AALBORG GFM37 flow meter included ±0.1 resolution, ±1.5% accuracy, and ±0.5% repeatability error, and was obtained following the RSS method as shown below in Equation (6) (Figliola & Beasely, 2006),

$$u_{tot} = \sqrt{u_{res}^2 + \sum u_i^2} = \sqrt{(0.05)^2 + Q^2\left(0.015^2 + 0.005^2\right)} \tag{6}$$

Since the AALBORG GFM37 flow meter was calibrated for argon gas the measurements were corrected using a k-factor as suggested by the manufacturer (AALBORG, 2009),

$$k_{gas} = \frac{1}{\rho c_p} \tag{7}$$

$$Q_{N_2} = Q_{Ar}\frac{k_{N_2}}{k_{Ar}} \tag{8}$$

The uncertainty was then propagated through Equation (9) to obtain the error for N_2 measurements,

$$u_{tot,N_2} = \sqrt{\left(u_{tot,Ar}\frac{\partial Q_{N_2}}{\partial Q_{Ar}}\right)^2} = u_{tot,Ar}\frac{k_{N_2}}{k_{Ar}} \quad (9)$$

Figure 11 shows the calibration chart obtained along with a linear least squares fit to the data and the results are summarized in Table 4 (see Appendix D for details on regression analysis). The results show that the indicated flow rate is slightly smaller than the actual flow rate. Fortunately, the flow rate indicated on the 3080 classifier is not directly communicated to the AIM software for calculation, but is a user specified value in the AIM software. Therefore the calibration chart will be used to translate between the indicated and actual, desired, flow rate.

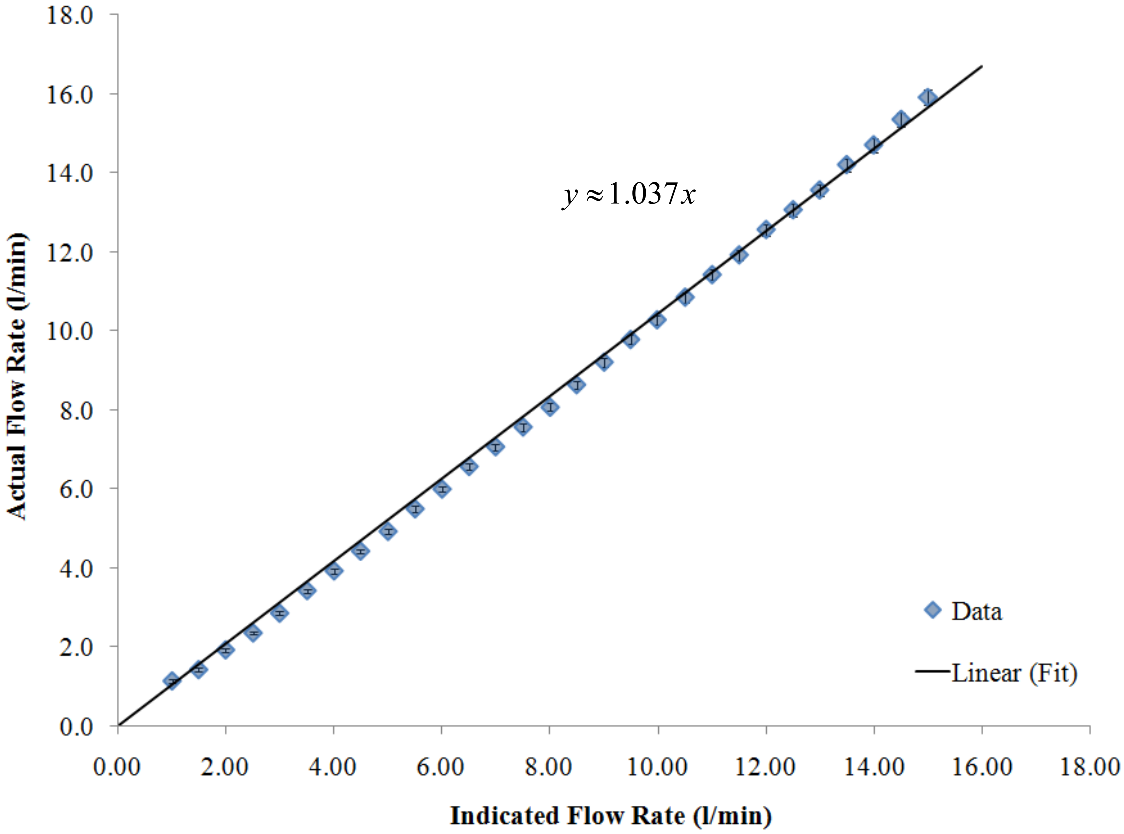

Figure 11. 3080 classifier sheath flow rate calibration chart.

Table 4

Linear-Least-Squares-Fit Regression Results for N_2 Calibration Curve

Gas	a	b	σ_b	$\delta y_{95\%}$	n	ν	R^2
N_2	0	1.037	0.004	0.4	29	28	0.998

Sheath flow rate selection

The 3071A & 3080 sheath flow rates were selected by ensuring that the chosen flow rates aligned the measurable particle size range with the expected particle size range. This was done using Equation (1) with the definition of electrical mobility to determine the minimum and maximum measurable particle diameters for a given sheath flow rate.

$$\overline{Z}_p = \frac{Q_{sh}}{2\pi VL} \ln\left({r_2}/{r_1} \right) \equiv \frac{qeC_c}{3\pi\mu d_p} \tag{10}$$

$$d_{p,\min} = \frac{2q_{\max} eC_c V_{\min} L}{3\mu Q_{sh} \ln\left({r_2}/{r_1} \right)} \tag{11}$$

$$d_{p,\max} = \frac{2q_{\min} eC_c V_{\max} L}{3\mu Q_{sh} \ln\left({r_2}/{r_1} \right)} \tag{12}$$

Since q_{max} is unknown, q_{min} (i.e. $q = 1$) was used to determine Q_{sh} based on the upper size limit which was previously determined for each material by measuring the size distributions using the SMPS spectrometer. The size distributions were averaged over multiple measurements and the results are shown for N_2 gas in Figure 12. The results indicate that measurements could be extended down to approximately 5 nm and also that

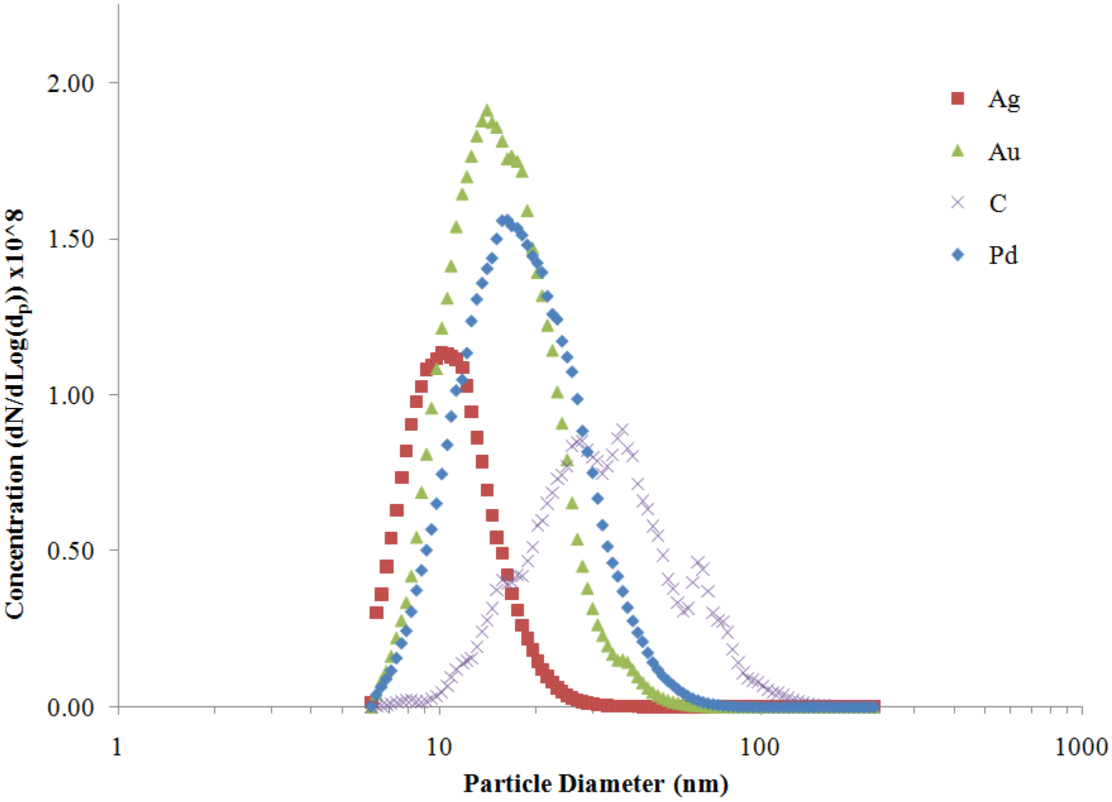

Figure 12. Typical particle size distributions in N_2 carrier gas obtained using SMPS spectrometer with Q_{sh} = 15(L/min) and Q_{poly} = Q_{mono} = 1.5 (L/min).

there are few particles above 220 nm. The 3071A sheath flow rate has an upper limit near 20 (L/min) which will be used based on these results to capture high mobility particles ($q > 1$) while maintaining capabilities for measuring particles over 200 nm. The 3080 classifier of the SMPS has a maximum flow rate of 15 (L/min) which will be used to capture particles down to ~5 nm (q = 1). The 3080 sheath flow rate can be lower than the 3071A since the majority of particles have obtained ±1 units of charge after passing through the charge neutralizer. Table 5 summarizes the conditions to be used during charged and neutral particle measurement including flow rates and voltage ranges. The voltage ranges are based on Equations (11) & (12) as well as the considerations described above. Recall that the TDMA uses air as the sheath gas within the 3071A and assuming little to no mixing of the sheath and aerosol flows inside the DMA, air is also supplied to the SMPS.

Table 5

Instrument Parameters Selected for Charged and Neutral Particle Measurements

$q = 1$	3071A				SMPS			
	Q_{sh} (L/min)	Voltage (kV)	$d_{p,min}$ (nm)	$d_{p,max}$ (nm)	Q_{sh} (L/min)	Voltage (kV)	$d_{p,min}$ (nm)	$d_{p,max}$ (nm)
TDMA	20	$-7 \le V \le 7$	4.91	157	15	$-(10 \le V \le 0.01)$	5.66	239
ESP					15	$-(10 \le V \le 0.01)$	5.76	244

Procedure

Charged Particle Measurement (TDMA)

Measurements began by powering on the SMPS, 3071A, GFG-1000, and the vacuum pump. N_2 gas was then supplied to the spark generator and its regulator was set to 1.2 bar (5 L/min), corresponding to the lowest operating setting. The 3071A sheath and polydisperse flow rates were then adjusted to the desired values, and since the SMPS maintains a constant aerosol sample flow rate, Q_{mono} remains constant from the 3071A classifier. To maintain consistency in particle concentrations between measurements with the TDMA and the ESP, the aerosol flow rates were set equal to each other ($Q_{poly} = Q_{mono}$). This is important because during charged particle measurement the TDMA acts as an "exchange" device, moving particles of selected mobility from one volume (Q_{poly}) to another (Q_{mono}). Since the SMPS measures size distributions in terms of particle concentration (i.e. #/cm^3) the volumes in which the particles are measured must be consistent. When using the ESP there is no “exchange” between volumes so the conditions seen between the two devices must be consistent to allow for data comparison. To equate the aerosol flow rates, Q_{mono} was first measured using the GFM37 and Q_{poly} was then set to match this value by using the GFM37 flow meter while adjusting the metering valve on the purge circuit shown in Figure 9a. Next, the sheath air flow rate was adjusted on the 3071A using the GFM37 flow meter and the built-in metering valve on the 3071A classifier. Based on the expected particle size range the metering valve was opened completely to maximize the sheath flow rate. All flow rates were recorded for use in the AIM software and for data analysis.

After setting the system flow rates the AIM software was initiated and the appropriate parameters were entered. First, a single scan with the SMPS was performed with no particle generation and the 3071A voltage off to check for random particle detection and possible contamination in the system. After verifying that the system was clean and free from contamination, particle generation was initiated and the 3071A was adjusted to the first stable voltage, approximately ±25 V. Three scans were then taken with the SMPS to obtain an average size distribution and once completed the voltage on the 3071A was adjusted to the next value determined by Equation (4) and the process was repeated. Scans were completed for all subsequent voltages within the range of the 3071A or until three consecutive scans resulted in no particles, signifying that the mobility limit has been reached and particles are no longer being classified by the 3071A. Once the testing was completed for both positive and negative voltages of the 3071A, the GFG-1000 was cleaned, new electrodes were installed, and the procedure was repeated for the new material. Table 6 below summarizes the experimental parameters used including the particle size range for the SMPS and the operating voltage range of the 3071A DMA.

Table 6

Experimental Parameters for Charged and Neutral Particle Measurements

Particle[a]	**SMPS range (nm)**[b]	**Measured range (nm)**[c]	**Operating voltage (V)**[d]
Graphite			
Negative	5.94 – 225	9.14 – 225	(32.61 – 6745)
Positive	5.94 – 225	9.47 – 225	- (22.41 – 6737)
Neutral	6.04 – 225	7.37 – 225	10,000
Graphite (with aggregate particle correction)			
Negative	5.94 – 225	10.2 – 225	(32.61 – 6745)
Positive	5.94 – 225	10.2 – 225	- (22.41 – 6737)
Neutral	6.04 – 225	10.2 – 225	10,000
Gold			
Negative	5.94 – 225	8.51 – 57.3	(32.61 – 1886)
Positive	5.94 – 225	7.37 – 68.5	- (23.42 – 2764)
Neutral	6.04 – 225	6.15 – 217	10,000
Silver			
Negative	5.94 – 225	8.20 – 35.9	(27.58 – 508.4)
Positive	5.94 – 225	7.64 – 41.4	- (22.41 – 1003)
Neutral	6.04 – 229	6.38 – 225	10,000
Palladium			
Negative	5.94 – 225	8.82 – 85.1	(32.61 – 4568)
Positive	5.94 – 225	7.64 – 102	- (22.41 – 5207)
Neutral	6.04 – 229	6.15 – 225	10,000

[a] $Q_{poly} = Q_{mono}$ = 1.4 l/min. [b] Measurable size range by SMPS. [c] Size range detected by SMPS. [d] Operating voltage refers to voltage range used on 3071A classifier during charged particle measurement and the voltage set on the ESP during neutral particle measurement.

Neutral Particle Measurement (ESP)

The neutral particle size distributions were obtained by connecting the ESP in-line with the SMPS as shown in Figure 9b. The flow rate through the ESP was then set to match the flow rate used during charge particle measurement with the TDMA by connecting the AALBORG GFM37 flow meter in-line with the ESP and adjusting the metering valve. Once the flow rate through the ESP was calibrated the AIM software was initiated and the appropriate parameters were entered in the software. N_2 gas properties were entered for the ESP measurements and the 3080 sheath flow calibration chart was also used to set the sheath flow rate. The ESP was then turned on and was operated at a voltage of 10 kV. A single scan was first performed with the SMPS with no particle generation to verify that the system was free from contamination. Particle generation was then initiated and three consecutive scans were performed to obtain an average size distribution as was done with the charged particle measurement.

Data Reduction

The TDMA technique directly measures the mobility-size distribution of the sampled aerosol and therefore needs to be transformed into a charge-size distribution using analytical techniques. A simple technique would be to use Equations (1) & (2) to define the centroid mobility and mobility width, respectively, with the definition of electrical mobility (Equation (10)) to separate the particle charges from the measured sizes at a given voltage. However this technique does not account for particle diffusion and spread of the transfer function which will cause overlap between adjacent mobility ranges. To account for these effects a lognormal approximation for the diffusing transfer function (Equation (14)) given by Stolzenburg and McMurry (2008) was used. The original diffusing transfer function developed by Stolzenburg (1988) was not used since it includes combinations of exponentials and error functions and is therefore less convenient for numerical searching. However the lognormal approximation has been shown to give comparable results with low relative error (Stolzenburg & McMurry, 2008).

The algorithm used to deduce the charge-size distribution from the mobility-size distribution data begins by examining a size distribution for a single DMA voltage. The centroid mobility is then calculated using the given flow rates and DMA voltage using Equation (1), which is then used to calculate the centroid diameters for each charge level q_1, q_2, q_3, …etc. using the definition of electrical mobility (Equation (10)). The diameter width at each charge level is then found with the lognormal transfer function by using the Newton-Raphson method to locate the upper and lower diameters at a defined cutoff value (since the lognormal transfer function is a continuous function with infinite domain). In this case a cutoff value of 0.001 was used corresponding to 0.1 % probability of transmission through the DMA. With the diameter widths determined for each charge level, the size distribution is then sorted into charge regions with the diameter widths marking transitions between charge levels. Since the lognormal transfer function accounts for particle diffusion the diameter widths can consequently overlap. The particle concentrations are additionally sorted in proportion to the magnitude of each transfer function of charge q_i at each particle diameter to determine the relative fractions associated with each charge level (see Figure 13). The particle concentrations can then be extracted with the corresponding particle diameter for each charge region, and the process repeated over all DMA voltages forming the charge-size distribution as described below in Equation (13). This algorithm was executed in Mathematica® to obtain the charge-size distributions for graphite, gold, palladium, and silver aerosol and an example of the program in given in Appendix E.

$$n(q_i,d_p)=\sum_{\bar{Z}_p}\sum_{d_p} n(\bar{Z}_p,d_p)\frac{\Omega(d_p,\bar{Z}_p,q_i)}{\sum_j \Omega(d_p,\bar{Z}_p,q_j)} \qquad (13)$$

$$\Omega(V,\tilde{D}_p)=\Omega(d_p,\bar{Z}_p,q)=\frac{M_{Dg0}}{\sqrt{2\pi\ln^2\sigma_{Dg}}}\exp\left[-\frac{1}{2}\frac{\left(\ln\tilde{D}_p-\ln\tilde{D}_{pg}\right)^2}{\ln^2\sigma_{Dg}}\right] \qquad (14)$$

In addition, the graphite data was treated with and without the Nanoparticle Aggregate Mobility Analysis AIM software module to correct the size distribution measurements for chain agglomerates. Note that this algorithm is not necessary for neutrally charged particles since the SMPS provides the size distribution directly.

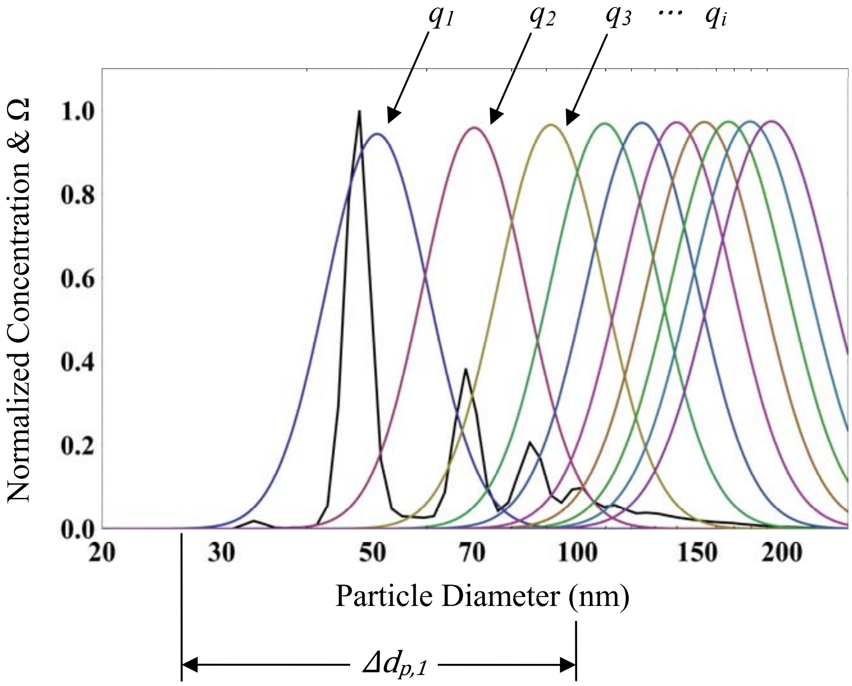

Figure 13. Depiction of data reduction procedure showing transfer functions for multiple charge levels with a typical size-mobility distribution.

Results

The charge-size distributions obtained from using the algorithm described in Equation (13) are shown in Figures 14–16 for carbon, carbon considering chain agglomerates with the Nanoparticle Aggregate Mobility Analysis module, gold, palladium, and silver aerosol. The carbon aerosols were analyzed up to ±10 units of charge and show roughly equal distributions of positive and negative charges up to a charge level of ±3, at which point the number of positively charged particles exceed the number of negatively charged particles. This trend continues with increased charge with the difference becoming greater with increased charge. The neutral size distribution covers the broadest range of particle diameters and also shows the highest number concentration over the entire diameter range except for a small region near the peak of the singly charged particle distributions. Analyzing the graphite particles as chain agglomerates slightly flattened the original distributions, raising the number concentrations slightly at diameters above and below the peak concentration. In addition, the minimum particle diameter was shifted higher to 10 nm which was specified as the average primary particle diameter for the chain agglomerates determined from the TEM image for graphite shown in Figure 5.

Gold, palladium and silver showed similar results as the graphite with higher concentrations of positive charges than negative charges with the differences becoming very apparent at increasing charge levels and the neutral size distribution showing the highest concentration over the entire diameter range. Silver had significant charges up to ±4 units of charge and had the least amount of spread between positive and negative charges. Silver also had the smallest charged particle diameter range extending just beyond 40 nm. The neutral size distribution however extended over a range beyond 100 nm.

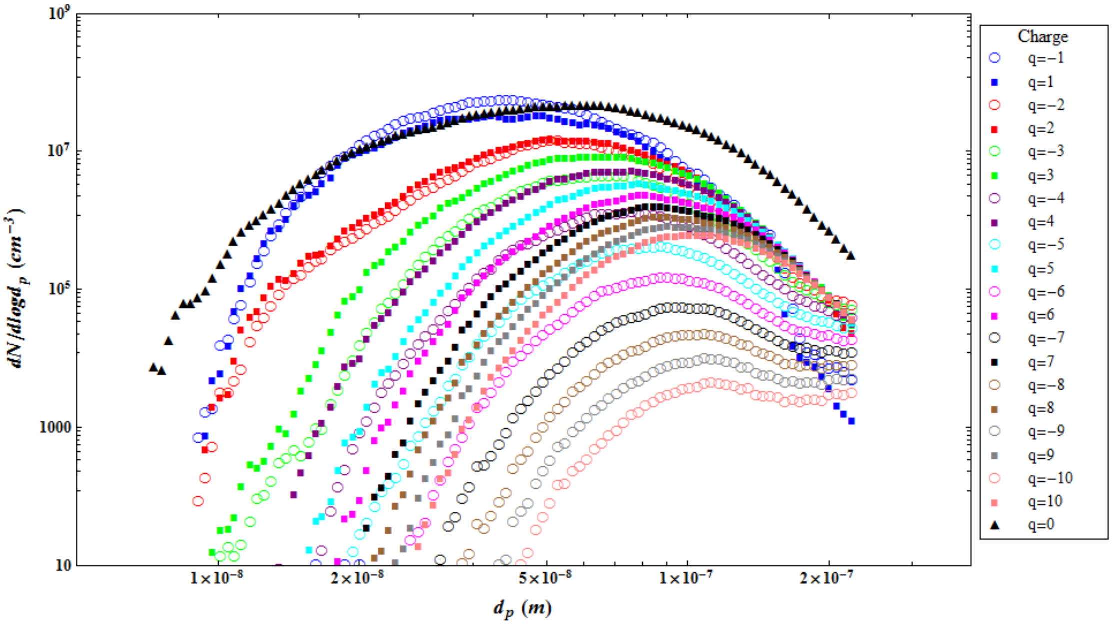

(a)

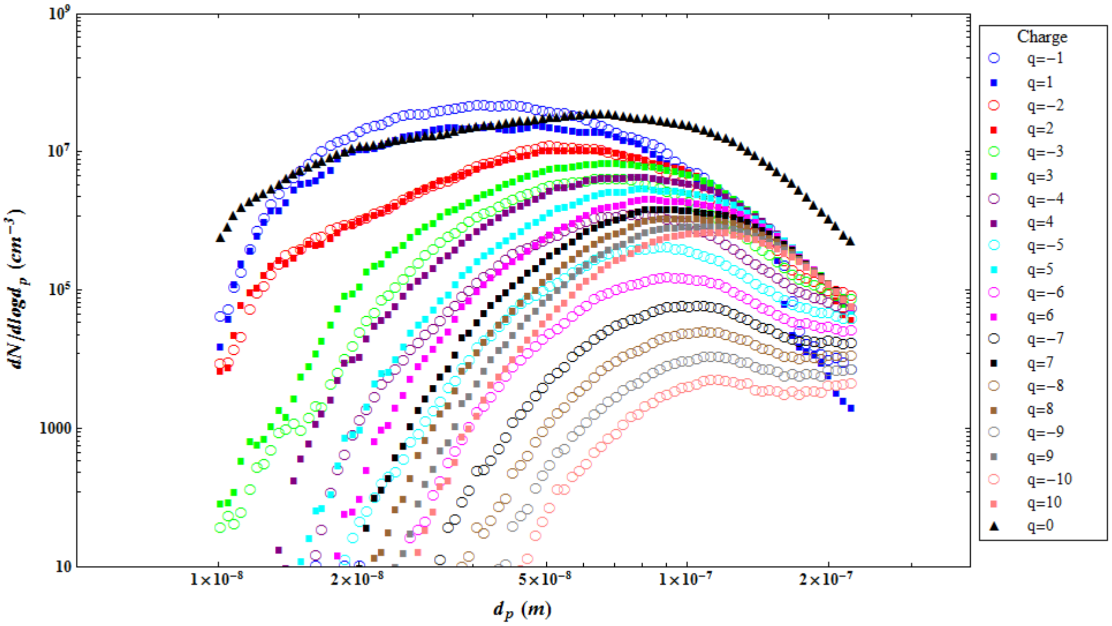

(b)

Figure 14. Charge-size distributions for spark generated (a) graphite and (b) graphite considered as chain agglomerates.

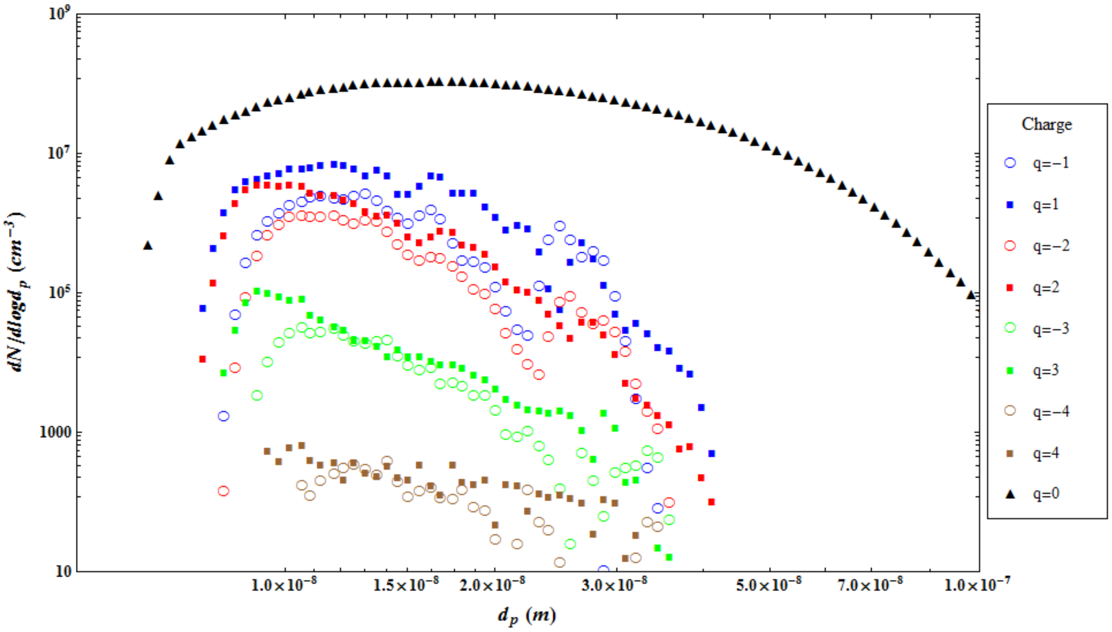

(a)

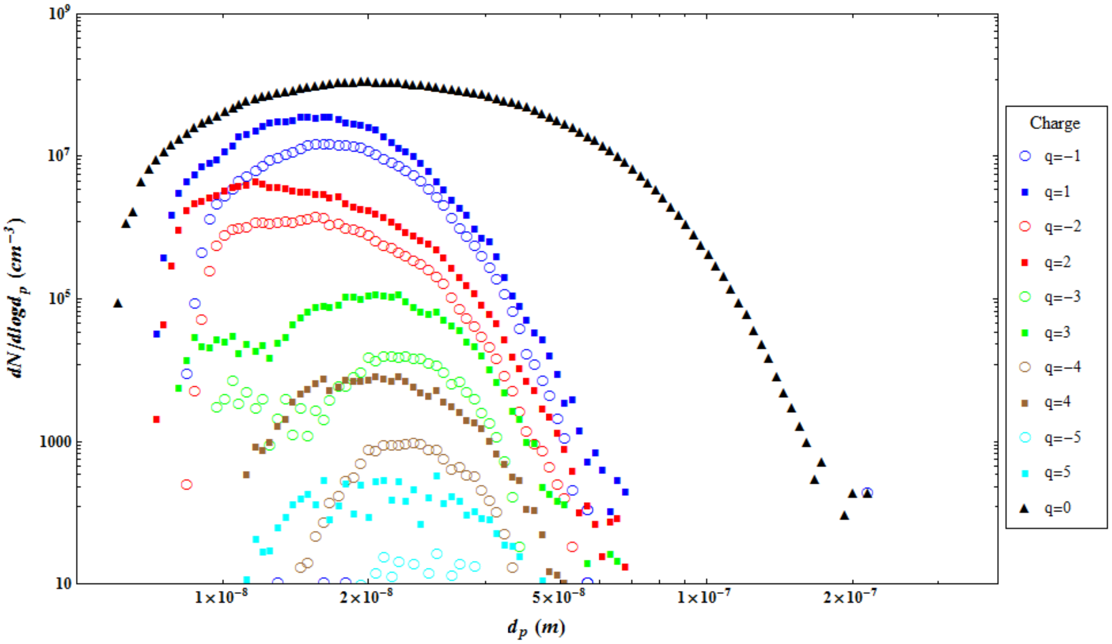

(b)

Figure 15. Charge-size distributions for (a) silver and (b) gold spark generated aerosol.

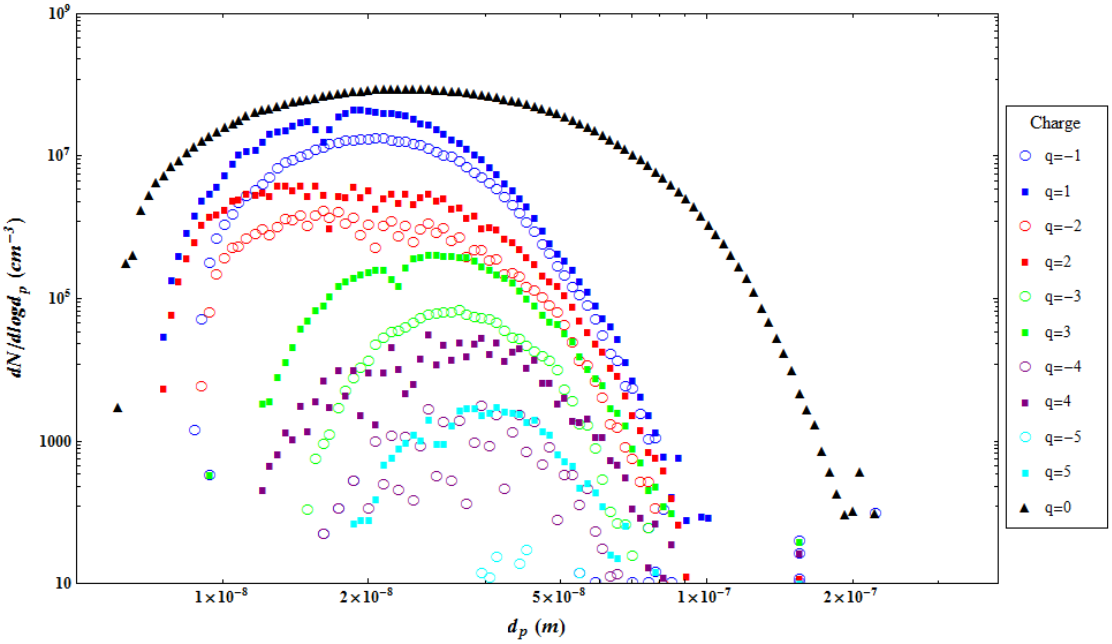

Figure 16. Charge-size distribution for palladium spark generated aerosol.

Gold was found to have charges up to ±5 units of charge with the charge diameter range extending up to 70 nm and the neutral size distribution extending up to 200 nm. Palladium was also found to have significant charges up to ±5 units of charge with the charge particle diameter extending up to 100 nm and the neutral size distribution extending up to 200 nm. As previously mentioned, both gold and palladium showed higher concentrations of positively charged particles and the difference between the positive and negative charge distributions increased with increased charge level. At high charge levels the difference could be as high as two orders of magnitude. A summary of the results is given in Appendix F including the maximum particle concentration and the size range for all results pictured in Figures 14–16.

Discussion

Particle charge and size distributions have been obtained for spark generated graphite, gold, silver, and palladium nanoparticles using a TDMA apparatus in conjunction with an ESP. The results show large concentrations of neutral particles over a large range of particle diameters, existence of multiple charges within all generated aerosols, and charge asymmetry with higher concentrations of positively charge particles than negative at the same charge level. The later is not representative of the typically expected equilibrium charge distribution described by Fuchs (1963) and Wiedensohler (1986) with charge asymmetry favored by negatively charged particles, however charge equilibrium is not necessarily expected because of the particle generation process and the short time between generation and measurement.

It is postulated that when the carrier gas is ionized during the spark generation process negative ions are lost to the electric current leaving the carrier gas with an abundance of positive gas phase ions. In addition, since the electric current is mostly due to mobility of negative gas phase ions the majority of metallic vapor is expected to be produced from the spallation from the cathode and therefore the vapor leaving the cathode will assume a positive charge. The gas phase ions are largely responsible for driving charge equilibrium and in the presence of equal concentrations of positive and negative ions the particle charge distribution will favor negative charges because negative ions typically have higher mobilities (Friedlander, 2000). However, in the present case with a diminished number of negative ions the particle charge distribution will be driven instead by the abundance of positive ions. The ability of the TDMA apparatus used here to accurately measure particle charge-size distributions may be better confirmed by using a radioactive charge neutralizer immediately after the spark generator to confirm or refute the ability of the apparatus to measure the expected equilibrium charge distribution. Unfortunately this was not possible during the duration of this project because a second charge neutralizer was unavailable.

The results given here provide additional support toward the use of the TDMA technique in characterizing charged aerosols, especially those without origins in combustion processes. The TDMA and ESP instruments established from this work will also allow for additional experimental research in charged aerosol and fission product transport studies at NSEI including characterization of aerosols associated with VHTRs and the nuclear source term.

References

Clement, C.F., Clement, R. A., Harrison, R. G. (1995). Charge distributions and coagulation of radioactive aerosols. Journal of Aerosol Science, 26(8), 1207–1225.

Clement, C. F., Harrison, R. G. (1992). The charging of radioactive aerosols. Journal of Aerosol Science, 23(5), 481–504.

Clement, C. F., Harrison, R. G. (2000). Enhanced localized charging of radioactive aerosols. Journal of Aerosol Science, 31(3), 363–378.

Cleveland, J. C. (1985). ORNL analysis of AVR performance and safety. Proceedings of A Specialists' Meeting on Safety and Accident Analysis for Gas-Cooled Reactors, May 13–15, IAEA-TECDOC-358, 73–84.

Dietrich, G., Neumann, W., Roehl, N. (1997). Decommissioning of the thorium high temperature reactor (THTR 300). Technical committee meeting on technologies for gas cooled reactor decommissioning, fuel storage and waste disposal, September 8–10, IAEA-TECDOC-1043, 9–15.

Emets, E. P., Kascheev, V. A., Poluektov, P. P. (1991). Simultaneous measurement of aerosol particle charge and size distributions. Journal of Aerosol Science, 22(3), 389–394.

Everett, M. R., Kinsey, D. V., Römberg, E. (1966). Carbon Transport Studies for Helium Cooled High Temperature Reactors. D. P. 491, November.

Figliola, R. S., & Beasley, D. E. (4th). (2006). Theory and Design for Mechanical Measurements. Hoboken, NJ, USA: John Wiley & Sons, Inc.

Friedlander, S. K. (2^{nd}) (2000). Smoke, Dust, and Haze: Fundamentals of Aerosol Dynamics. New York, NY, USA: Oxford University Press, Inc.

Fuchs, N. A. (1963). On the stationary charge distribution on aerosol particles in a bipolar ionic atmosphere. Pure and Applied Geophysics, 56 (1), 185–193.

Fuller, C. H. (1988). Fort Saint Vrain operational experience. Technical committee on design requirements, operation and maintenance of gas-cooled reactors, September 21–23, IWGGCR-19, 55–61.

Gensdarmes, F., Boulaud, D., & Renoux, A. (2001). Electrical charging of radioactive aerosols—comparison of the Clement-Harrison models with new experiments. Journal of Aerosol Science, 32, 1437–1458.

Ghosh, T. K., & Prelas, M. A. (2009). Energy Resources and Systems Vol. 1: Fundamentals and Non-Renewable Resources. Springer Science + Business Media B.V.

IAEA (1997). Fuel performance and behavior in gas cooled reactors. International Atomic Energy Agency, November 1997, IAEA-TECDOC-978.

Kadak, A. C. (2005). A future for nuclear energy: pebble bed reactors. Int. J. Critical Infrastructures, 1(4), 330–345.

Kim, S. H., Woo, K. S., Liu, B. Y. H., Zachariah, M. R. (2005). Method of measuring charge distribution of nanosized aerosols. Journal of Colloid and Interface Science, 282, 46–57.

Kingrey, K. I. (2003). Fuel summary for Peach Bottom unit 1 high-temperature gas-cooled reactor cores 1 and 2. Idaho National Engineering and Environmental Laboratory, April 2003, INEEL/EXT-03-00103.

Knutson, E. O. (1971*). The distribution of electric charge among the particles of an artificially charged aerosol* (Doctoral dissertation). Retrieved from ProQuest. (Publication # AAT 7227767, ProQuest ID: 761244981)

Knutson, E. O., Whitby, K. T. (1975). Aerosol classification by electric mobility: Apparatus, theory, and applications. Journal of Aerosol Science, 6, 443–451.

Kugeler, K., Stulgies, A., & Epping, Ch. (1988). Aerosol formation during water ingress into the core of a pebble bed high-temperature reactor. Aerosol Science and Technology, 9, 177–187.

Krüger, K. J., Ivens, G. P. (1985). Safety-related experiences with the AVR reactor. Proceedings of A Specialists' Meeting on Safety and Accident Analysis for Gas-Cooled Reactors, May 13–15, IAEA-TECDOC-358, 61–70.

Lyons, L. (1993). A Practical Guide to Data Analysis for Physical Science Students. New York, NY, USA: Cambridge University Press.

Maricq, M. M. (2005). The dynamics of electrically charged soot particles in a premixed ethylene flame. Combustion and Flame, 141, 406–416.

Maricq, M. M. (2006). A comparison of soot size and charge distributions from ethane, ethylene, acetylene, and benzene/ethylene premixed flames. Combustion and Flame, 144, 730–743.

Maricq, M. M. (2006). On the electrical charge of motor vehicle exhaust particles. Journal of Aerosol Science, 37, 858–874.

Mariqc, M. M. (2008). Bipolar diffusion charging of soot aggregates. Aerosol Science and Technology, 42, 247–254.

Mariqc, M. M. (2008). Thermal equilibrium of soot charge distributions by coagulation. Journal of Aerosol Science, 39, 141–149.

Moormann, R. (2008). Fission product transport and source terms in HTRs: Experience from AVR pebble bed reactor. Science and Technology of Nuclear Installations. Doi:10.1155/2008/597491

Morris, R. N. (2008). Next Generation Nuclear Plant Phenomena Identification and Ranking Tables (PIRTs) - Volume 3: Fission-Product Transport and Dose PIRTs. U.S. Nuclear Regulatory Commission, October 2007, NUREG/CR-6944, Vol. 3.

Navadi, W. (2nd). (2008). Statistics for Engineers and Scientists. New York, NY: McGraw-Hill.

PALAS (2003). GFG-1000 Graphite Aerosol Generator Operating Manual. PALAS® GmbH, March 2003.

PBMR (2010). Fuel Element Design for PBMR. Retrieved from http://www.pbmr.co.za /contenthtml/pictureFX/imgcache/00000047.jpg

Roellig, K. (1990). The THTR-300 coolant gas activity, an indicator of fuel performance. Proceedings of a specialists' meeting on behavior of gas cooled reactor fuel under accident conditions, November 5–8, IWGGCR-25, 99–108.

Simones, M. P., Gutti, V. R., Meyer, R. M., Loyalka, S. K. (2011). Measurements of aerosol charge and size distribution: graphite, gold, palladium, and silver nanoparticles. Accepted for publication in Nuclear Technology.

Stempniewicz, M. M., Komen, E. M. J., & de With, A. (2008). Model of particle re-suspension in turbulent flows. Nuclear Engineering and Design, 238, 2943–2959.

Takamatsu, K., Nakagawa, S., & Takeda, T. (2006). Development of core dymanics analysis of coolant flow reduction tests of HTTR. Proceedings HTR2006: 3rd International Topical Meeting of High Temperature Reactor Technology, October 1–4, 2006, Johannesburg, South Africa.

TSI (1994). Model 3071A Electrostatic Classifier Instruction Manual. TSI Incorporated, Revision B, Part Number: 1933765.

TSI (2007). Model 3776 Ultrafine Condensation Particle Counter Operation and Service Manual. TSI Incorporated, Revision C, Part Number: 1980522.

TSI (2008). Series 3080 Electrostatic Classifiers Operation and Service Manual. TSI Incorporated, Revision H, Part Number: 1933792.

U.S. Department of Energy (2002). A technology roadmap for Generation IV nuclear energy systems. U.S. DOE Nuclear Energy Research Advisory Committee and the Generation IV International Forum, December 2002, GIF-002-00.

Venneri, F. (2005). Deep-burn: Destruction of nuclear waste and recycle of resources using MHR technology. IAEA. Retrieved from http://www.iaea.org/inisnkm/nkm /aws/fnss/fulltext/ictp2005_Gudowski_Trieste-2005_DB.pdf

Wichner, R. P. (1991). Fission product plateout and liftoff in the MHTGR primary system: A review. Oak Ridge National Laboratory, NUREG/CR-5647,ORNL/TM-11685, R1, R7, R8.

Wiedensohler, A., Lutkemeier, M., Feldpausch, Helsper, C. (1986). Investigation of the bipolar charge distribution at various gas conditions. Journal of Aerosol Science, 17 (3), 413–416.

Yeh, H. C., Newton, G. J.,Raabe, O. G., Boor, D. R. (1976). Self-charging of 198Au-labeled monodisperse gold aerosols studied with a miniature electrical mobility spectrometer. Journal of Aerosol Science, 7, 245–253.

Yeh, H. C., Newton, G. J., Teague, S. V. (1978). Charge distribution on plutonium-containing aerosols produced in mixed-oxide reactor fuel fabrication and the laboratory. Health Physics, 35, 500–503.

Appendix A

Electrostatic Precipitator

A parallel plate ESP was designed and constructed to allow the size distribution of neutrally charged particles to be measured. When used, the ESP is connected in place of the 3071A classifier and removes charged particles from the aerosol flow before entering the SMPS spectrometer.

Design

In designing the ESP the following design criteria were identified:

- Dimensions and features
    - Able to collect particles ≤ 300 nm
    - Simple, compact, and portable
    - Uniform flow over collector plates
    - Easy to machine (prevent complex geometries and features)
    - Airtight seal
    - Easy disassembly for cleaning
    - Dimensions align with standard sizes of bulk material

- Material Selection
    - Mechanical properties
    - Machinable
    - Ability to withstand mechanical stresses from gas pressure
    - Electrical insulator in excess of 10 kV
    - Readily available
    - Affordable

The general ideation was a two piece design with a main lower body and a removable cover. Both pieces would be machined from a solid insulating material and contain recessed metal collection plates. The cover would be bolted in place and include an o-ring seal to make an airtight chamber. The material chosen based on its mechanical and electrical properties was high density polyethylene (HDPE) and the chamber dimensions were aligned with the standard sizes of HDPE available to minimize cost and waste during machining.

The internal dimensions of the ESP were chosen based on the ability to collect particles with the lowest expected electrical mobility (i.e. 300 nm particles with a single charge). To examine the dependence of each variable a simple two-dimensional model was used as shown below in Figure A1 along with the following assumptions:

- Streamlines are parallel to the x-axis
- Initially particles are moving along streamlines at terminal velocity ($v_x = Q/A$)
- Particles quickly reach terminal velocity (Stokes region)
- Gas velocity independent of height (flat velocity profile)
- Electric field is everywhere vertical, perpendicular to streamlines
- Gravitational settling and diffusion losses negligible

Motion in the x-direction is straightforward with no applied forces and motion in the y-direction is given as a balance between the aerodynamic drag and electrostatic forces. The aerodynamic drag force (F_D) can be represented in terms of the electrical mobility of the particle and will be balanced by the electrostatic force (F_E),

$$m\frac{d^2x}{dt^2} = 0 \tag{A1}$$

$$m\frac{d^2y}{dt^2} = F_D - F_E = \left(\frac{qe}{Z_p}\right)\left(-\frac{dy}{dt}\right) - \left(qeE\right) = -\left(\frac{qe}{Z_p}\right)\frac{dy}{dt} - \left(\frac{qeV}{d}\right) \approx 0 \tag{A2}$$

Equations (A1) & (A2) can both be readily solved using separation of variables,

$$m\frac{d^2x}{dt^2} = 0 \quad \Rightarrow \quad \frac{dx}{dt} = v_x = \frac{Q}{A} \quad \Rightarrow \quad \underline{\underline{x(t) = \left(\frac{Q}{A}\right)t + x_0}} \tag{A3}$$

$$-\left(\frac{qe}{Z_p}\right)\frac{dy}{dt} - \left(\frac{qeV}{d}\right) = 0 \quad \Rightarrow \quad \frac{dy}{dt} = -\frac{Z_pV}{d} \quad \Rightarrow \int_{y_0}^{y} dy = -\frac{Z_pV}{d}\int_0^t dt$$

$$\Rightarrow \quad \underline{\underline{y(t) = y_0 - \frac{Z_pV}{d}t}} \tag{A4}$$

This result also follows directly from the definition of Z_p,

$$Z_p = -\frac{1}{E}\frac{dy}{dt} \quad \Rightarrow \quad \frac{dy}{dt} = -\frac{Z_pV}{d} \quad \Rightarrow \quad \int_{y_0}^{y} dy = -\frac{Z_pV}{d}\int_0^t dt \quad \Rightarrow \quad \underline{\underline{y(t) = y_0 - \frac{Z_pV}{d}t}}$$

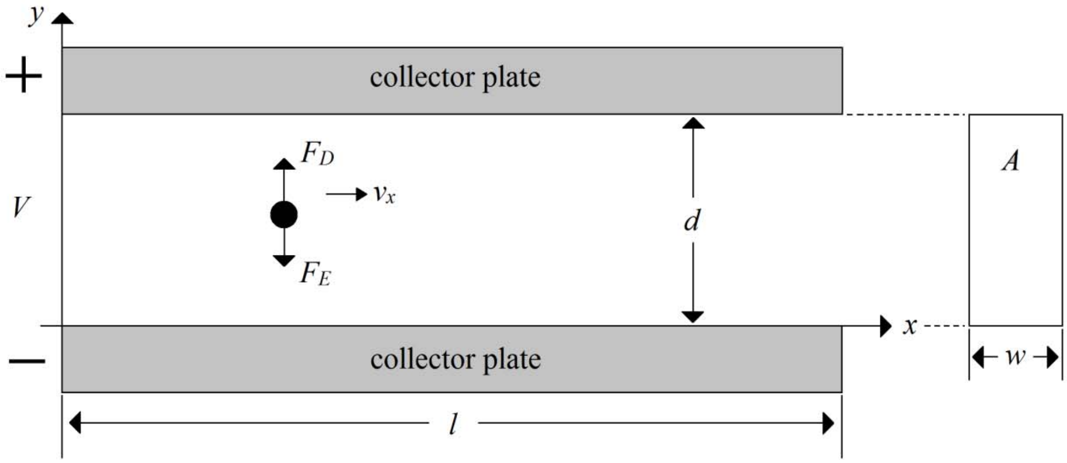

Figure A1. Two-dimensional model of ESP.

Since the vertical velocity is inversely proportional to the separation distance, the smallest allowable value of *d* was chosen to provide fast particle collection. This was constrained to 0.5 in. (1.27 cm) by the 1/8 in. NPT fittings used for the gas inlet and outlet ports. Using Equations (A3) & (A4) parametrically the trajectory of a 300 nm singly charged particle was approximated at various plate widths to determine the plate length required as shown in Figure A2. The simulation assumed the particle was initially located at the opposite plate ($y = d$) when entering the collecting region representing the longest particle path. The Reynolds number (*Re*) was also calculated as a function of plate width as shown in Figure A2 to ensure laminar flow over collector plates. Flow in the laminar regime will maintain the accuracy of model assumptions and reduce particle resuspension. The *Re* for non-circular ducts is given by Incropera and DeWitt (2006) in terms of the hydraulic diameter,

$$D_H = \frac{4A}{P} \tag{A5}$$

$$\mathrm{Re} = \frac{QD_H}{\nu A} = \frac{4Q}{\nu P} = \frac{2Q}{\nu\left(w+d\right)} \tag{A6}$$

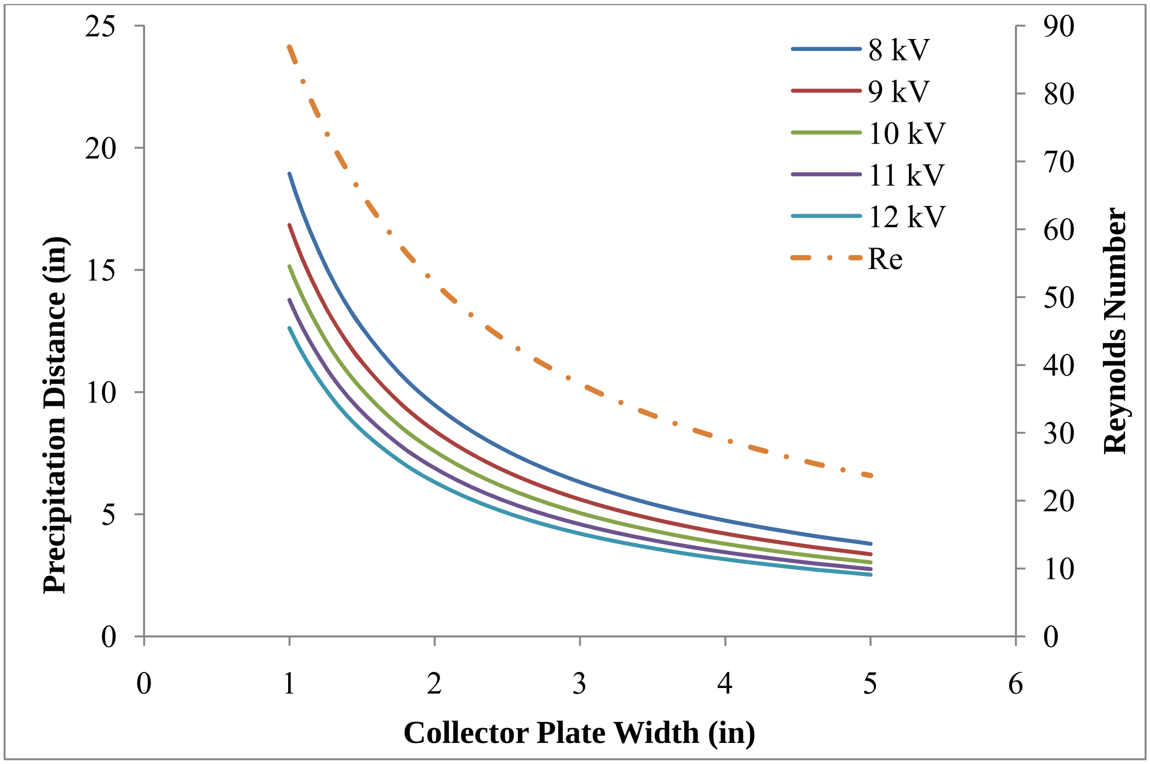

Figure A2. Precipitation distance and Reynolds number as a function of collector plate width.

It is clear from Figure A2 that the flow over the collector plates is laminar and well below the transition value of 2300. From these results a plate width of 2.5 in. (6.35 cm) was chosen based on a reasonable precipitation length, Reynolds number, and also the bulk sizes of material available.

To ensure the streamlines over the collection plates were linear, the transition region of the entering flow was modeled using FLUENT software as shown in Figure A3. Based on the results recirculation zones span 2 inches past the transition region of the chamber, therefore the collection plates will be offset by this distance.

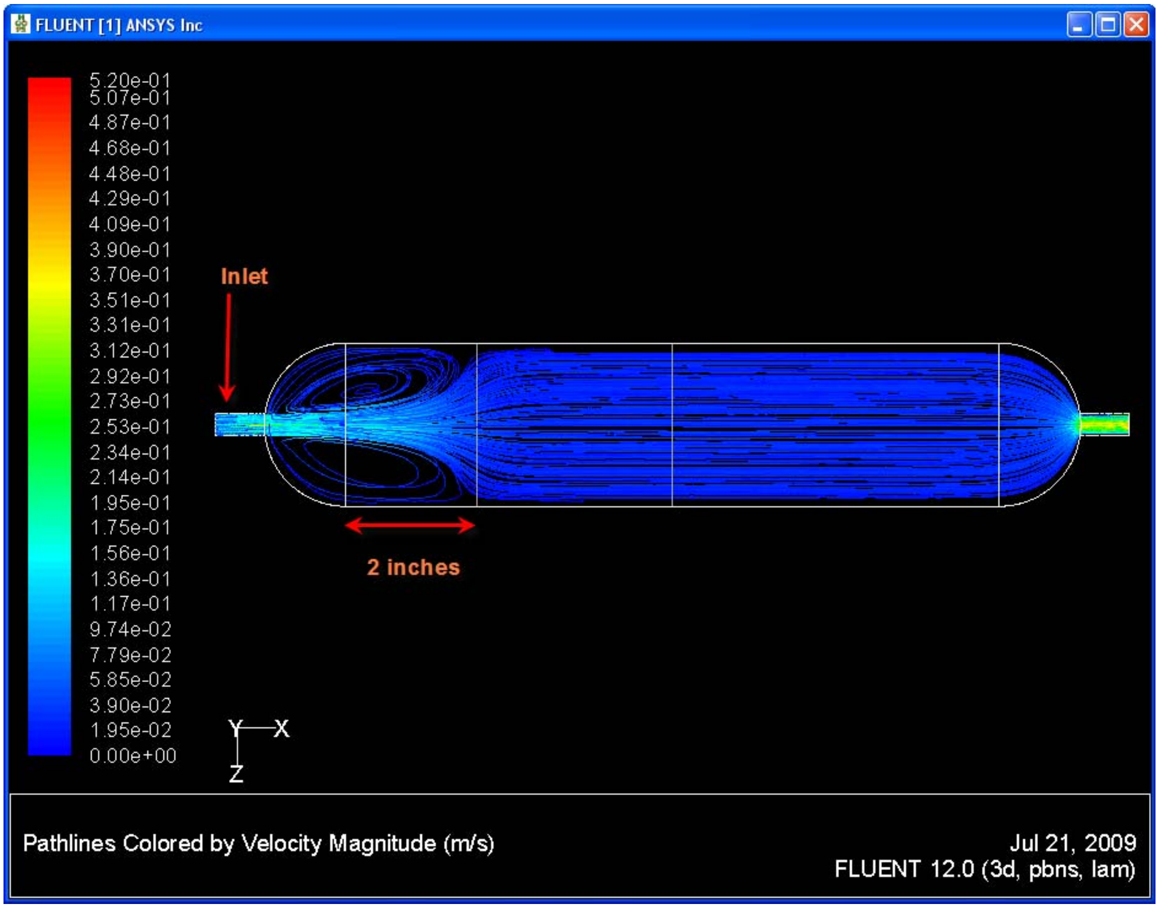

Figure A3. CFD analysis of fluid flow within collection chamber
(courtesy of Dr. Veera Rajesh Gutti, NSEI).

Engineering drawings and exploded views of the final design are shown in Figures A4–A7. Apart from the ESP chamber a Spellman High Voltage supply and an Omron AC/DC converter was selected with the help of Dr. Ryan Meyer at NSEI, and all of the components were mounted into an aluminum chassis.

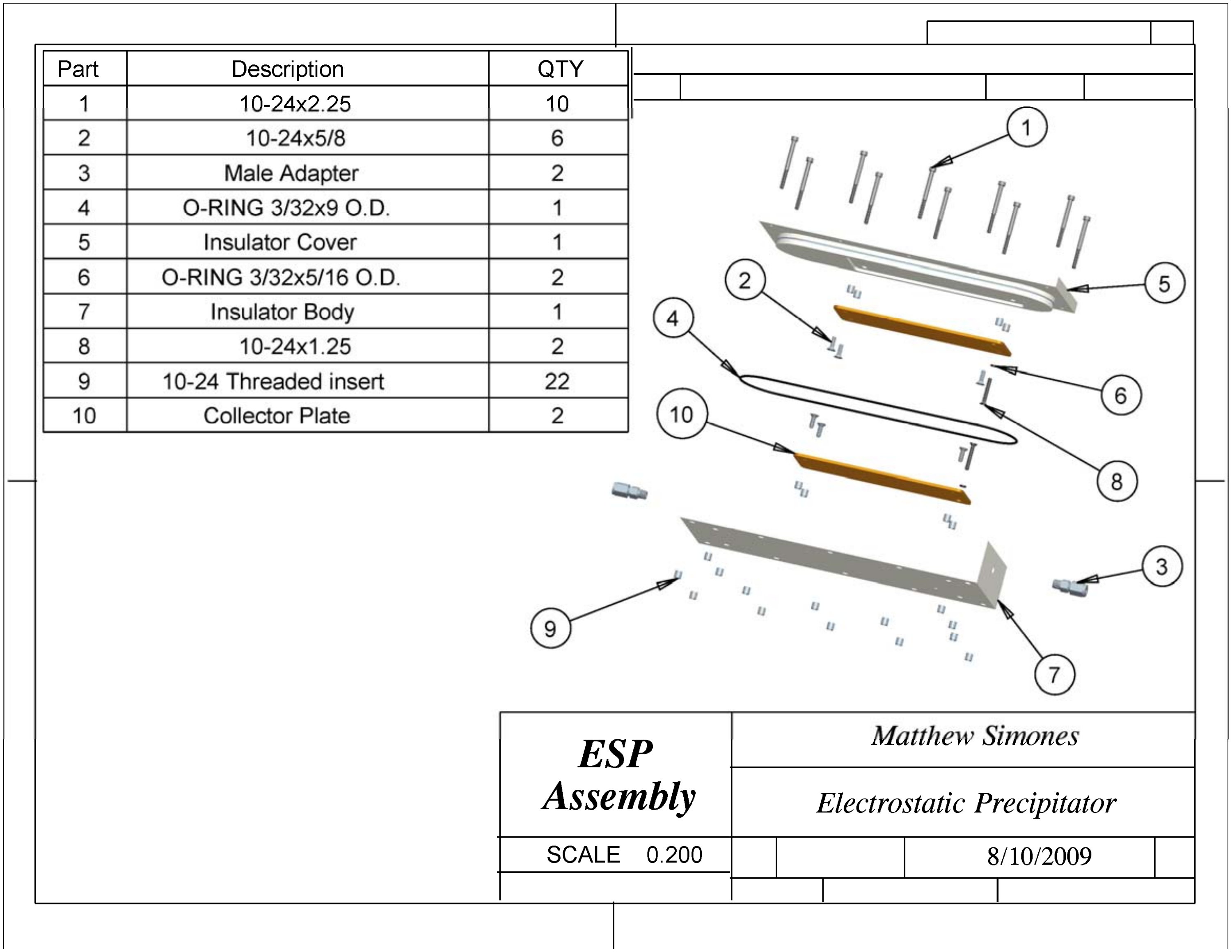

Part	Description	QTY
1	10-24x2.25	10
2	10-24x5/8	6
3	Male Adapter	2
4	O-RING 3/32x9 O.D.	1
5	Insulator Cover	1
6	O-RING 3/32x5/16 O.D.	2
7	Insulator Body	1
8	10-24x1.25	2
9	10-24 Threaded insert	22
10	Collector Plate	2

Figure A4. Assembly drawing of electrostatic precipitator
(scaled down from letter size to fit on page).

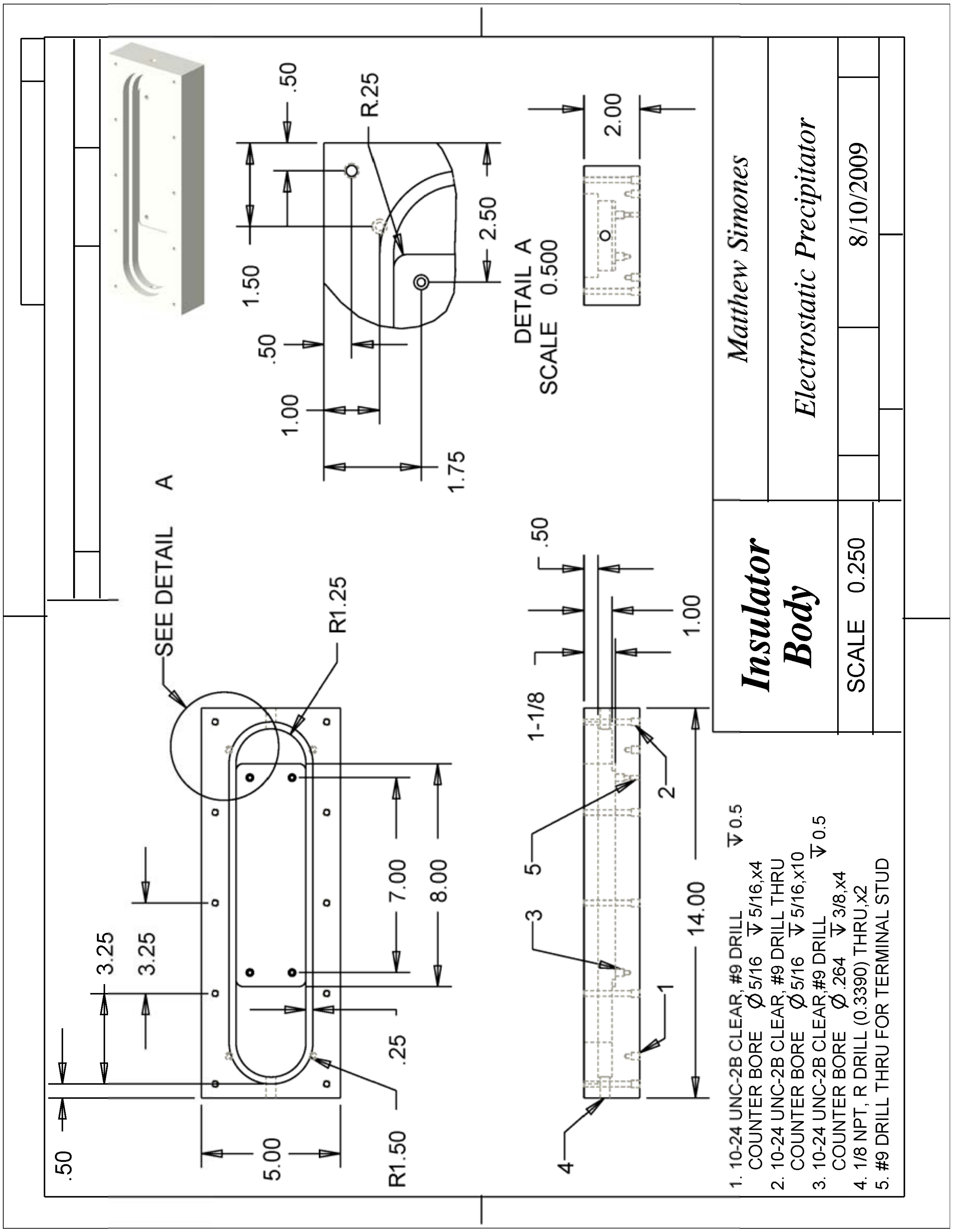

Figure A5. Detailed engineering drawing of electrostatic precipitator insulator body (scaled down from letter size to fit on page).

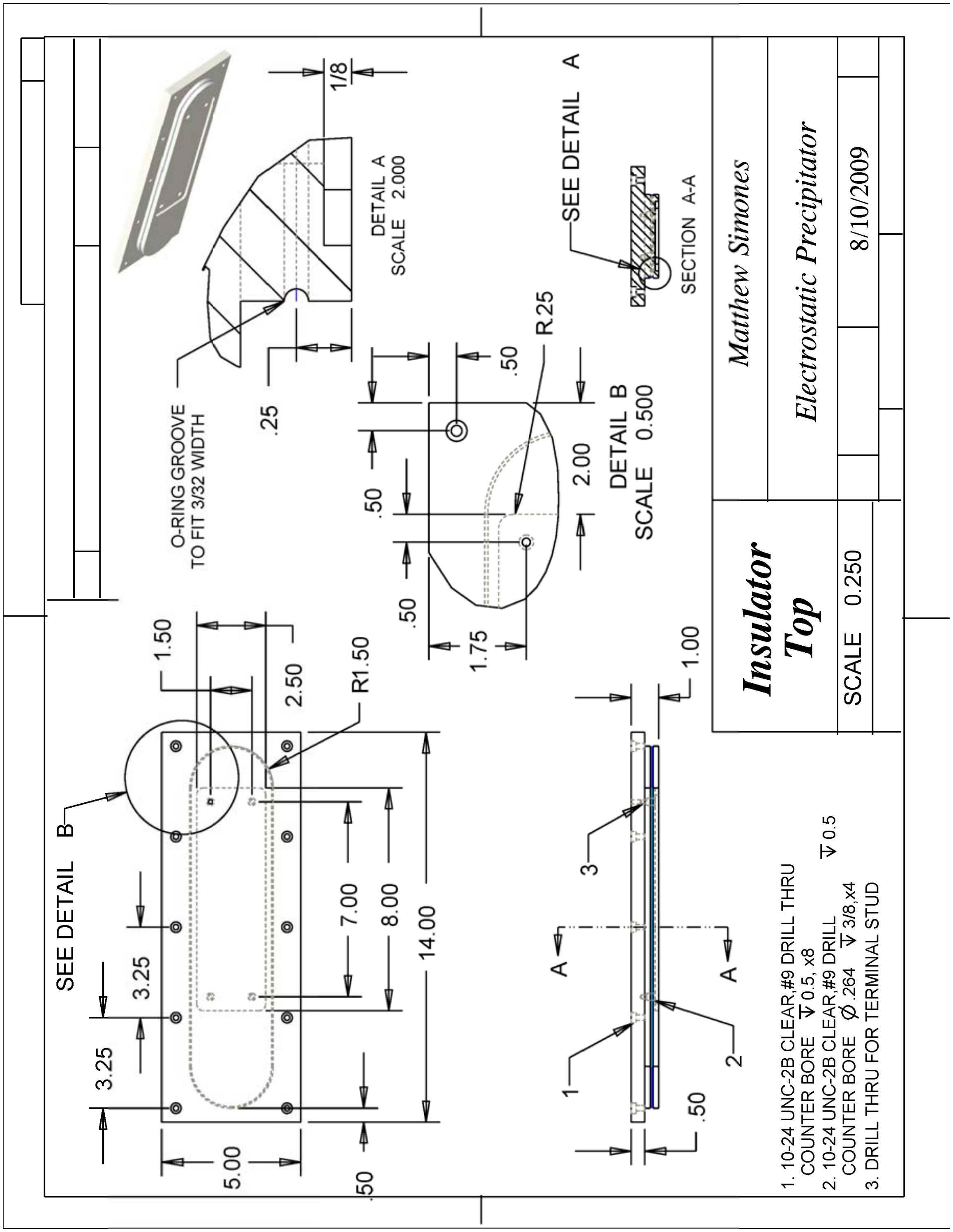

1. 10-24 UNC-2B CLEAR,#9 DRILL THRU
   COUNTER BORE ↧0.5, x8
2. 10-24 UNC-2B CLEAR,#9 DRILL ↧0.5
   COUNTER BORE ⌀.264 ↧3/8,x4
3. DRILL THRU FOR TERMINAL STUD

Figure A6. Detailed drawing of electrostatic precipitator insulator top
(scaled down from letter size to fit on page).

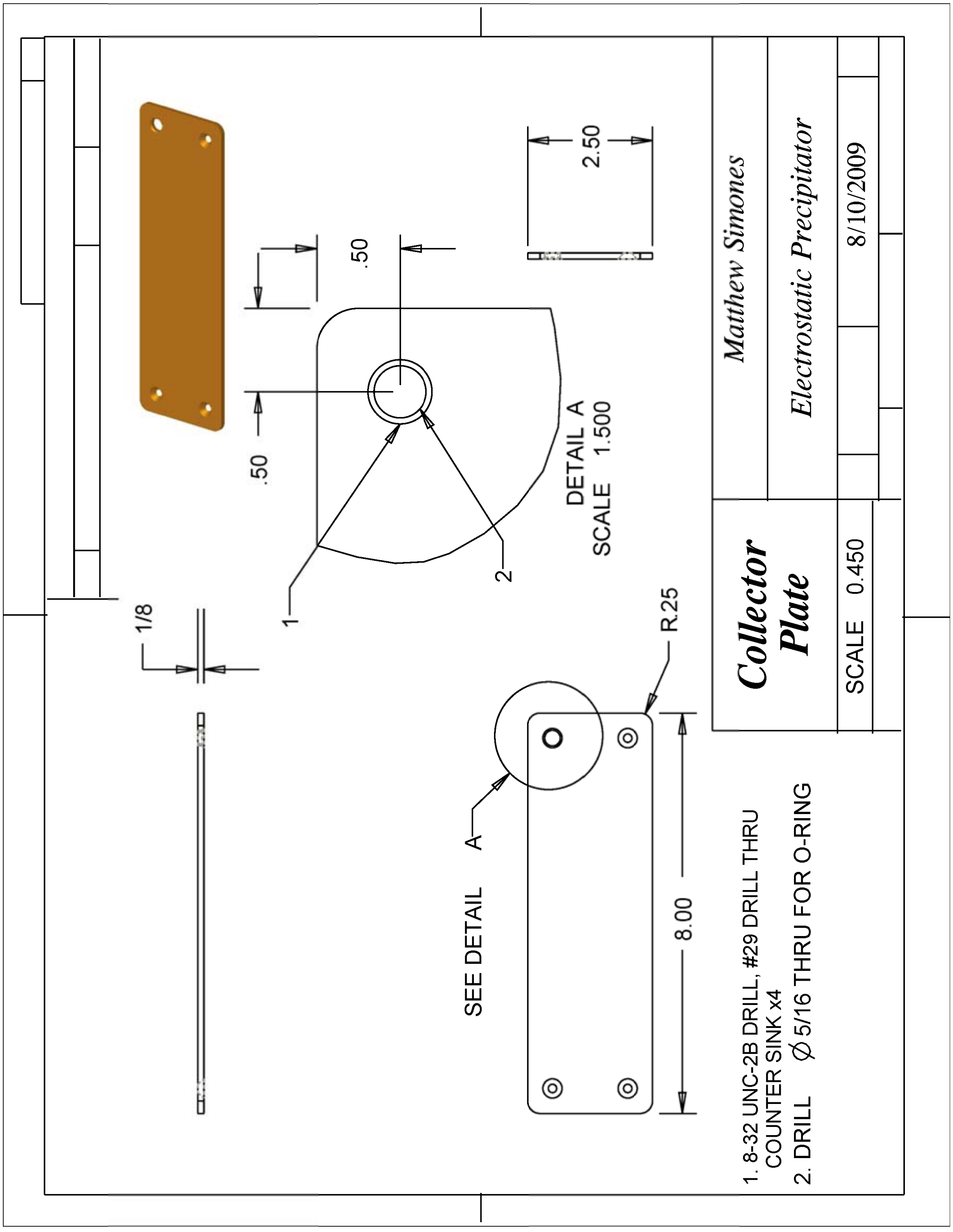

Figure A7. Detailed drawing of electrostatic precipitator collector plate (scaled down from letter size to fit on page).

Calibration

The ESP was calibrated to determine the particle collection efficiency as a function of voltage across the collector plates. This was done using the SMPS spectrometer with the radioactive neutralizer removed so that charged particles that are not filtered by the ESP can be classified and counted. The neutral particles which pass through the ESP unaffected will remain neutrally charged inside the SMPS and will not be classified. Particle collection efficiency was carried out for carbon, palladium, silver, and gold nanoparticles generated by the GFG-1000 spark generator with N_2 Carrier gas. Figure A9 shows that the ESP is nearly 100% efficient at collecting charged particles for all four types of aerosol at collector plate voltages above ~7 kV. To ensure high collection efficiency the ESP will be maintained at or above 10 kV.

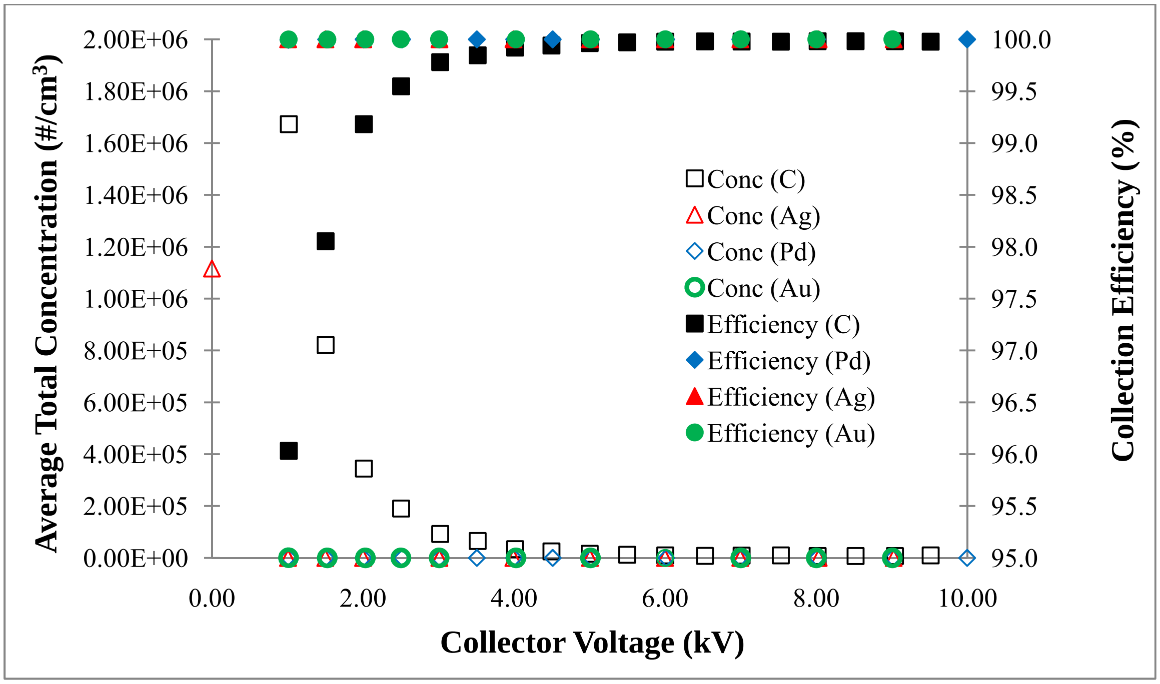

Figure A8. Average total charged particle concentration and ESP collection efficiency versus ESP collector plate open voltage for graphite, palladium, silver, and gold aerosol in N_2 carrier gas.

Appendix B

3071A Digital Voltage Indicator Calibration Data

Table B1

3017A Indicated and Measured Positive DMA Voltages with Associated Uncertainty

V_{ind}	V_{act}	$\sigma_{act}{}^{a}$	V_{ind}	V_{act}	σ_{act}	V_{ind}	V_{act}	σ_{act}
	(V)			(V)			(kV)	
10	17.42	0.349	400	**411**	**8.2**	2.500	2.520	.0504
20	27.77	0.556	450	460	9.2	2.750	2.777	.0556
30	37.88	0.758	500	512	10.2	3.000	3.020	.0604
40	**47.3**	**0.95**	550	561	11.2	3.250	3.279	.0656
50	57.9	1.16	602	613	12.3	3.507	3.533	.0707
60	67.9	1.36	649	660	13.2	3.734	3.760	.0752
70	77.7	1.55	699	711	14.2	4.023	4.050	.0810
80	88.0	1.76	751	764	15.3	4.255	**4.29**	**0.086**
90	98.3	1.97	800	813	16.3	4.512	4.54	0.091
100	108.1	2.16	850	863	17.3	4.774	4.80	0.096
120	128.5	2.57	899	912	18.2	5.040	5.07	0.102
140	149.0	2.98	949	963	19.3	5.237	5.27	0.106
160	168.5	3.37	1000	1015	20.3	5.547	5.58	0.112
180	189.3	3.79	1250	1266	25.3	5.726	5.76	0.115
200	208.8	4.18	1500	1521	30.4	6.075	6.11	0.122
250	260.1	5.20	1750	1770	35.4	6.541	6.57	0.132
300	309.8	6.20	2000	2025	40.5	7.110	7.14	0.143
350	360.0	7.20	2250	2274	45.5	7.365	7.39	0.148

Note. Bold values indicate changes in DMM resolution
[a]*Based on design stage uncertainty*

Table B2

3017A Indicated and Measured Negative DMA Voltages with Associated Uncertainty

V_{ind}	V_{act}	σ_{act}^{a}	V_{ind}	V_{act}	σ_{act}	V_{ind}	V_{act}	σ_{act}
	(V)			(V)			(kV)	
-10	-3.28	0.066	-400	-396.6	7.93	-2.5	-2507	50.2
-20	-13.34	0.267	-449	**-446**	**8.9**	-2754	-2762	55.3
-30	-23.58	0.472	-500	-497	9.9	-3007	-3015	60.3
-40	-33.52	0.671	-549	-546	10.9	-3244	-3253	65.1
-50	**-43.9**	**0.88**	-600	-597	11.9	-3507	-3515	70.3
-60	-53.7	1.08	-651	-649	13.0	-3724	-3733	74.7
-70	-64.0	1.28	-700	-698	14.0	-4000	-4009	80.2
-80	-74.1	1.48	-749	-747	14.9	-4222	**-4230**	**85**
-90	-84.0	1.68	-799	-798	16.0	-4542	-4550	91
-100	-94.4	1.89	-851	-849	17.0	-4736	-4750	95
-120	-114.4	2.29	-901	-900	18.0	-5028	-5040	101
-140	-134.3	2.69	-950	-950	19.0	-5233	-5240	105
-160	-155.0	3.10	-1000	-1000	20.0	-5532	-5540	111
-180	-175.0	3.50	-1250	-1251	25.0	-5752	-5760	115
-200	-194.6	3.89	-1503	-1506	30.1	-6052	-6060	121
-250	-245.6	4.91	-1750	-1753	35.1	-6554	-6560	131
-300	-295.1	5.90	-2000	-2005	40.1	-7060	-7070	142
-350	-345.8	6.92	-2254	-2260	45.2			

Note. *Bold values indicate changes in DMM resolution*

[a] *Based on design stage uncertainty*

Appendix C

3080 Sheath Flow Meter Calibration Data for N_2 Gas

Table C1

3080 Indicated and Measured Sheath Flow Rates for N_2 Gas

Q_{ind}	Q_{act}	σ_{act}
(L/min)		
1.00	0.7	0.04
1.49	1.1	0.04
1.99	1.4	0.04
2.50	1.8	0.04
2.99	2.1	0.04
3.50	2.5	0.05
4.00	2.8	0.05
4.49	3.2	0.05
5.00	3.6	0.05
5.50	3.9	0.06
6.00	4.3	0.06
6.50	4.6	0.06
6.99	5.0	0.07
7.50	5.3	0.07
8.00	5.7	0.07
8.49	6.0	0.08
9.00	6.4	0.08
9.49	6.7	0.08
9.98	7.1	0.09
10.50	7.5	0.09
11.00	7.8	0.09
11.50	8.2	0.10
12.00	8.5	0.10
12.50	8.9	0.11
12.99	9.2	0.11
13.49	9.6	0.11
13.99	9.9	0.12
14.50	10.3	0.12
15.00	10.7	0.13

Appendix D

Linear Regression (Least Squares Method)

In developing calibration curves linear regression, namely the least squares method, was used to fit a line to the data. Lyons (1993) gives a procedure for the least square method with unequal error as,

$$y = a + bx \tag{D1}$$

$$b = \frac{[1][xy] - [x][y]}{[1][x^2] - [x][x]} \tag{D2}$$

$$a = \langle y \rangle - b\langle x \rangle = \frac{[x^2][y] - [x][xy]}{[1][x^2] - [x][x]} \tag{D3}$$

$$\sigma_a^2 = \frac{[x^2]}{[1][x^2] - [x]} \tag{D4}$$

$$\sigma_b^2 = \frac{[1]}{[1][x^2] - [x]} \tag{D5}$$

$$[f] = \sum \frac{f_i}{\sigma_i^2} \tag{D6}$$

$$\langle f \rangle = \frac{[f]}{[1]} \tag{D7}$$

$$S_{\min} = \sum \frac{(a + bx_i - y_i)^2}{\sigma_i^2} \tag{D8}$$

The goodness-of-fit can also be estimated using the coefficient of determination (R^2) (Navidi, 2008),

$$R^2 = \frac{\sum (y_i - \bar{y})^2 - \sum (a + bx_i - y_i)^2}{\sum (y_i - \bar{y})^2} \tag{D9}$$

Appendix E

Mathematica Program Example

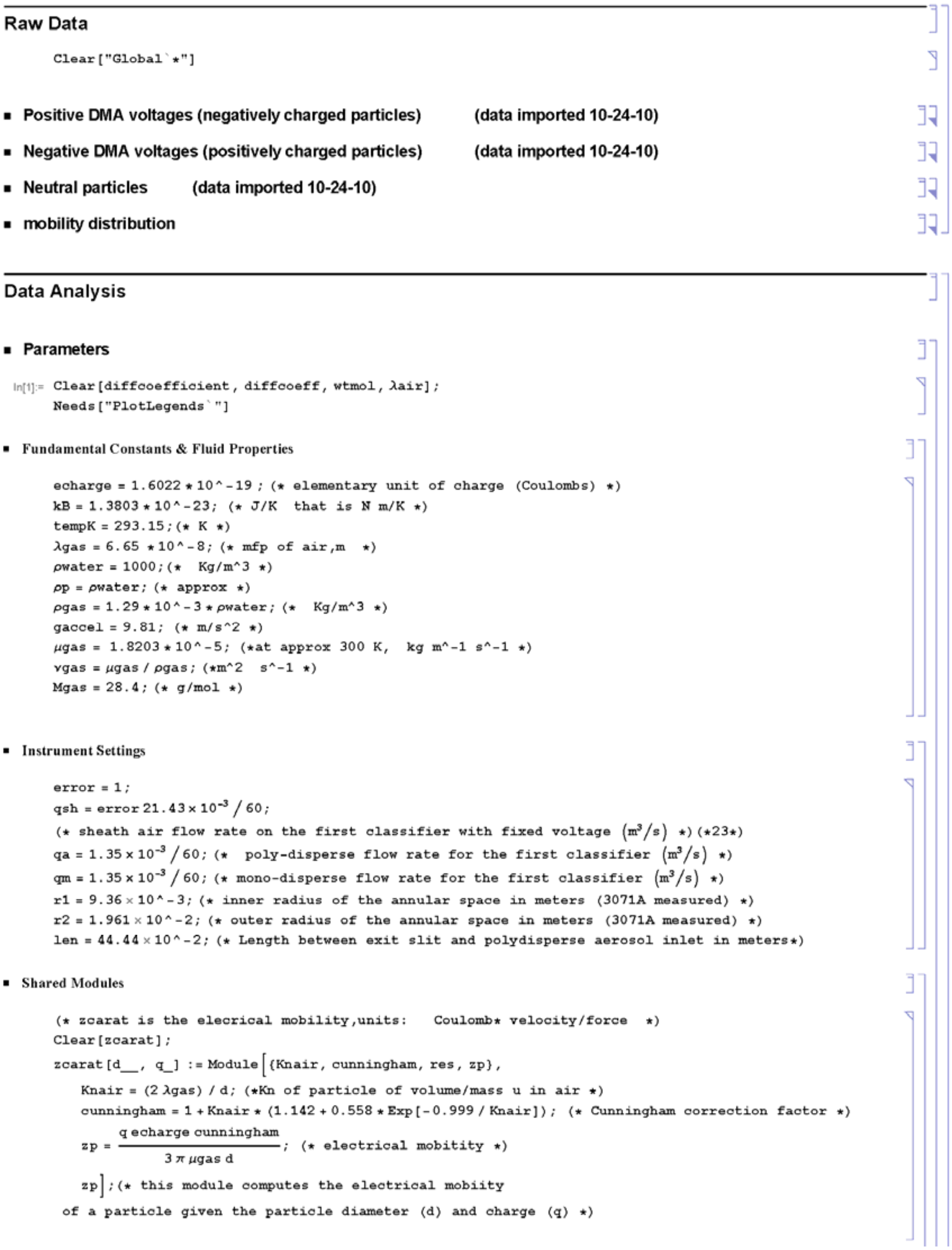

Raw Data

```
Clear["Global`*"]
```

- Positive DMA voltages (negatively charged particles) (data imported 10-24-10)
- Negative DMA voltages (positively charged particles) (data imported 10-24-10)
- Neutral particles (data imported 10-24-10)
- mobility distribution

Data Analysis

- Parameters

```
In[1]:= Clear[diffcoefficient, diffcoeff, wtmol, λair];
        Needs["PlotLegends`"]
```

- Fundamental Constants & Fluid Properties

```
echarge = 1.6022 * 10^-19 ; (* elementary unit of charge (Coulombs) *)
kB = 1.3803 * 10^-23; (* J/K  that is N m/K *)
tempK = 293.15;(* K *)
λgas = 6.65 *10^-8; (* mfp of air,m  *)
ρwater = 1000;(*  Kg/m^3 *)
ρp = ρwater; (* approx *)
ρgas = 1.29 * 10^-3 * ρwater; (*  Kg/m^3 *)
gaccel = 9.81; (* m/s^2 *)
μgas =  1.8203 * 10^-5; (*at approx 300 K,  kg m^-1 s^-1 *)
νgas = μgas / ρgas; (*m^2  s^-1 *)
Mgas = 28.4; (* g/mol *)
```

- Instrument Settings

```
error = 1;
qsh = error 21.43 × 10^-3 / 60;
(* sheath air flow rate on the first classifier with fixed voltage (m^3/s) *)(*23*)
qa = 1.35 × 10^-3 / 60; (*  poly-disperse flow rate for the first classifier (m^3/s) *)
qm = 1.35 × 10^-3 / 60; (* mono-disperse flow rate for the first classifier (m^3/s) *)
r1 = 9.36 × 10^-3; (* inner radius of the annular space in meters (3071A measured) *)
r2 = 1.961 × 10^-2; (* outer radius of the annular space in meters (3071A measured) *)
len = 44.44 × 10^-2; (* Length between exit slit and polydisperse aerosol inlet in meters*)
```

- Shared Modules

```
(* zcarat is the elecrical mobility,units:   Coulomb* velocity/force  *)
Clear[zcarat];
zcarat[d__, q_] := Module[{Knair, cunningham, res, zp},
   Knair = (2 λgas) / d; (*Kn of particle of volume/mass u in air *)
   cunningham = 1 + Knair * (1.142 + 0.558 * Exp[-0.999 / Knair]); (* Cunningham correction factor *)
        q echarge cunningham
   zp = ---------------------; (* electrical mobitity *)
             3 π μgas d
   zp]; (* this module computes the electrical mobiity
 of a particle given the particle diameter (d) and charge (q) *)
```

```
diallowandhigh[zi_, q_] := Module[{dd, d},
   dd = FindRoot[D[Ω[d, zi, q], d] == 0, {d, 10^-9, 1000 10^-9}][[1, 2]];
   reslow = FindRoot[Ω[d, zi, q] == 0.001, {d, dd - dd / 10, 10^-10, dd}][[1, 2]];
   reshigh = FindRoot[Ω[d, zi, q] == 0.001, {d, dd + dd / 10, dd, 1000 10^-9}][[1, 2]];
   {reslow, reshigh}];


Clear[Ω];
Ω[dp_, Zpstar_, charge_] := Module[{β, δ, σstar, GDMA, Dbar, Dpstar, ϰ, ϒ, ωa, ωs,
    A, Ig, Cs, DD, MDg0, lnDbarpg, lnσDg, astar, (*Zpstar*), Zp, Dp, Dpbar, DDpbar},
   β = (qm + qa)/(qa - qm + 2 qsh);
   δ = (qm - qa)/(qm + qa);
   ϰ = len r2/((r2^2 - r1^2));
   ϒ = (r1/r2)^2;
   A = Sqrt[1 - ϒ]/((1+ϒ)/2 Log[ϒ] + 1 - ϒ);
   Cs[dia_] = 1 + (2 λgas)/dia (1.142 + 0.558 E^(-.999 dia/(2 λgas))); (* cunningham slip correction *)
   DD[dia_] = (kB tempK Cs[dia])/(3 π μgas dia); (* diffusion coefficient *)
   Dbar[dia_] = (4 π len DD[dia])/(qa - qm + 2 qsh);

   Zp[dia_] = (charge echarge Cs[dia])/(3 π μgas dia);

   Dpstar = FindRoot[Zp[dpstar] == Zpstar, {dpstar, 10 × 10^-9, 10^-9, 1000 × 10^-9}][[1, 2]];

   Dpbar[dia_] = dia / Dpstar;

   astar = -D[Log[Zp[ddp], ddp], ddp] ddp /. ddp → Dpstar;


   F[ω_] := (((1-ω)^2 Log[ϒ])/(2 (1-ϒ)) + ω Log[ω] + (1 - ω))/(((1 + ϒ) Log[ϒ]/2 + (1 - ϒ)));
   ωa := FindRoot[F[ω] - (β (1 - δ))/(2 (1 + β)) == 0, {ω, .99}][[1, 2]];
   ωs := FindRoot[1 - F[ω] - (β (1 + δ))/(2 (1 + β)) == 0, {ω, .99}][[1, 2]];

   Ig[ω_] :=
    A^2/(1 - ϒ) (-ω^2 ((1 - ϒ) Log[ω] - (1 - ω) Log[ϒ])^2/2 + (ω^2 (1 - ϒ)/2 + ω^3 Log[ϒ]/3) ((1 - ϒ) Log[ω] - (1 - ω) Log[ϒ]) +
       (1 - ω^2) (1 - ϒ)^2/4 + 5 (1 - ω^3) (1 - ϒ) Log[ϒ]/18 + (1 - ω^4) (Log[ϒ])^2/12);

   GDMA = (4 (1 + β)^2 (Ig[ωs] - Ig[ωa]) + (ωa-ωs)/ϰ^2)/(1 - ϒ);
   σstar = Sqrt[GDMA Dbar[Dpstar]];

   MDg0 = β (1 + δ) / astar;
   lnDbarpg = -σstar^2 / astar;
   lnσDg = Sqrt[(β^2 (1 + δ^2)/6 + σstar^2 (1 + 2 σstar^2)) / astar^2];
```

```
    ΩΩ[DDpbar_] = MDg0 / Sqrt[2 π (lnσDg)^2] E^(-1/2 (Log[DDpbar] - lnDbarpg)^2/(lnσDg)^2);
    ΩΩ[Dpbar[dp]]];
Clear[selectlistqs];
selectlistqs[ii_] := Module[
   {dialimits, listjunk1, nlistq1, nlistq2, nlistq3, nlistq4, nlistq5, nlistq6, x, y, correction},
   dialimits = Map[diallowandhigh[Zplist[[ii -1]]](*,deltaZplist[[ii-1]]*) , #] &,
     {1, 2, 3, 4, 5, 6}];
   (* creates array of upper and lower diameter limits for q=1,2,3,4 *)

   (* listjunk1 is simply picking out the ii set of data, for a given ii (the mobility),
   the diameter and the corresponding value of the distribution  *)
   listjunk1 = Table[{datalist[[i, 1]], datalist[[i, ii]]}, {i, Length[datalist]}];
   (* for moblity zii with all charges *)
   (* creates lists of diameter and corresponding # value for each voltage (mobility) value *)
   error = Table[Sum[Ω[listjunk1[[i, 1]], Zplist[[ii - 1]], j], {j, 1, 6, 1}], {i, Length[listjunk1]}];

   (* Now select those with charge 1 *)
   nlistq1 = Table[If[dialimits[[1, 1]] <= listjunk1[[i, 1]] ≤ dialimits[[1, 2]], (*listjunk1[[i]]*)
      {listjunk1[[i, 1]], listjunk1[[i, 2]] * Ω[listjunk1[[i, 1]], Zplist[[ii - 1]], 1] / error[[i]]},
      {listjunk1[[i, 1]], 0}], {i, Length[listjunk1]}];
   (* Determines if any of the diameters in each listjunnk1 list falls within the diameter
    range calculated using the zcarat module, if so the # of particles corresponding
    to that diameter is extracted from the list, otherwise the # is set to zero *)

   nlistq2 = Table[If[dialimits[[2, 1]] <= listjunk1[[i, 1]] ≤ dialimits[[2, 2]], (*listjunk1[[i]]*)
      {listjunk1[[i, 1]], listjunk1[[i, 2]] * Ω[listjunk1[[i, 1]], Zplist[[ii - 1]], 2] / error[[i]]},
      {listjunk1[[i, 1]], 0}], {i, Length[listjunk1]}];

   nlistq3 = Table[If[dialimits[[3, 1]] <= listjunk1[[i, 1]] ≤ dialimits[[3, 2]], (*listjunk1[[i]]*)
      {listjunk1[[i, 1]], listjunk1[[i, 2]] * Ω[listjunk1[[i, 1]], Zplist[[ii - 1]], 3] / error[[i]]},
      {listjunk1[[i, 1]], 0}], {i, Length[listjunk1]}];

   nlistq4 = Table[If[dialimits[[4, 1]] <= listjunk1[[i, 1]] ≤ dialimits[[4, 2]], (*listjunk1[[i]]*)
      {listjunk1[[i, 1]], listjunk1[[i, 2]] * Ω[listjunk1[[i, 1]], Zplist[[ii - 1]], 4] / error[[i]]},
      {listjunk1[[i, 1]], 0}], {i, Length[listjunk1]}];

   nlistq5 = Table[If[dialimits[[5, 1]] <= listjunk1[[i, 1]] ≤ dialimits[[5, 2]], (*listjunk1[[i]]*)
      {listjunk1[[i, 1]], listjunk1[[i, 2]] * Ω[listjunk1[[i, 1]], Zplist[[ii - 1]], 5] / error[[i]]},
      {listjunk1[[i, 1]], 0}], {i, Length[listjunk1]}];

   nlistq6 = Table[If[dialimits[[6, 1]] <= listjunk1[[i, 1]] ≤ dialimits[[6, 2]], (*listjunk1[[i]]*)
      {listjunk1[[i, 1]], listjunk1[[i, 2]] * Ω[listjunk1[[i, 1]], Zplist[[ii - 1]], 6] / error[[i]]},
      {listjunk1[[i, 1]], 0}], {i, Length[listjunk1]}];

   {nlistq1, nlistq2, nlistq3, nlistq4, nlistq5, nlistq6}];

totals[q_] := Module[{total, totallist},
   total = Table[Sum[resultsfulllistqs[[i, q]][[j, 2]], {i, 1, Length[resultsfulllistqs]}],
     {j, 1, Length[diameterlist]}];
   totallist = Transpose[{diameterlist, total}];
   totallist];
```

- **Positive Voltages (negatively charged particles)**

The program below takes the SMPS data given as size distribution data as a function of DMA rod voltage, and obtains the corresponding size and charge distributions for q=(-1,- 2,- 3, etc.).

```
Clear[voltagelist, datalist0, diameterlist, datalist, numberconcdata, Zplist, resultsfulllistqs]

voltagelist = Drop[rawdatapos[[1]], 1];
(* This extracts the voltages from the raw data: row #1 with the first
   element (blank entry) dropped. NOTE: voltage list must be absolute values!! *)
datalist0 = Drop[rawdatapos, 1];
(* Takes the raw data set and drops the first row. Gives
  rows with the particle diameter as the first element followed by the # of
  particles for each voltage. this gives Length(voltagelist)+1 row elements. *)
diameterlist = Table[datalist0[[i, 1]] 10^-9, {i, Length[datalist0]}];
(* creates an array of just the diameters from the data set: row i,
column 1. Also converted to (m) from (nm) *)
```

```
datalist = Table[If[j == 1, datalist0[[i, j]] * 10^-9, datalist0[[i, j]]],
   {i, Length[diameterlist]}, {j, Length[voltagelist] +1}] ;
(* Converts only the diameters (column 1) from (nm) to (m),
leaving all other elements the same *)
numberconcdata = Table[datalist[[i, j]], {i, 1, Length[datalist]}, {j, 2, Length[datalist[[1]]]}];
(* gives array of only the particle concentration data: rows 1→All & columns 2→All *)

TableForm[datalist, TableHeadings → {{}, Prepend[voltagelist "volts", "Particle Dia"]}];
(* Gives tabulated result for the "datalistgold" array with the "voltagelist" printed above *)
```

$$Zplist = \frac{(qsh + 0.5 * (qa - qm)) * Log[r2 / r1]}{2 \times Pi \times voltagelist \times len};$$

```
(* this computes the electrical mobility of the particles sampled by the first classifier
 using the classifier parameters, NOTE: Zplist is a matrix due to voltagelist *)

resultsfulllistqs = Map[selectlistqs[#] &, Range[2, Length[datalist[[1]]]]];
(* evaluates selectlistqs for all mobilities starting with the second
  column in datalistgold array (the first column is diameter values not # data)
  Note: the Map could only be carried out over one variable so the
    number of mobility elements was releated to the number of Zplist elements
    (i.e. Length[datalistgold[[1]]-1=Length[Zplist] or (40)-1=39 ) *)

totalresults = Map[totals[#] &, Range[1, 6]];
(* the above module is mapped over all charges (q) included in resultfulllistqs,
creating a size distribtution for each charge q *)


charge1list = Partition[Riffle[Flatten[totalresults[[1]]], -1, 3], 3];
charge2list = Partition[Riffle[Flatten[totalresults[[2]]], -2, 3], 3];
charge3list = Partition[Riffle[Flatten[totalresults[[3]]], -3, 3], 3];
charge4list = Partition[Riffle[Flatten[totalresults[[4]]], -4, 3], 3];
charge5list = Partition[Riffle[Flatten[totalresults[[5]]], -5, 3], 3];
charge6list = Partition[Riffle[Flatten[totalresults[[6]]], -6, 3], 3];
chargelisttot =
  Flatten[{charge1list, charge2list, charge3list, charge4list, charge5list, charge6list}, 1];
(* each charge list appends the number of charges to the list, all lists are then combined *)


datalist1pos = Table[{charge1list[[i, 1]], charge1list[[i, 2]]}, {i, 1, Length[charge1list]}];
datalist2pos = Table[{charge2list[[i, 1]], charge2list[[i, 2]]}, {i, 1, Length[charge2list]}];
datalist3pos = Table[{charge3list[[i, 1]], charge3list[[i, 2]]}, {i, 1, Length[charge3list]}];
datalist4pos = Table[{charge4list[[i, 1]], charge4list[[i, 2]]}, {i, 1, Length[charge4list]}];
datalist5pos = Table[{charge5list[[i, 1]], charge5list[[i, 2]]}, {i, 1, Length[charge5list]}];
datalist6pos = Table[{charge6list[[i, 1]], charge6list[[i, 2]]}, {i, 1, Length[charge6list]}];

newlist1pos =
  Table[{charge1list[[i, 3]], charge1list[[i, 1]], charge1list[[i, 2]]}, {i, 1, Length[charge1list]}];
newlist2pos = Table[{charge2list[[i, 3]], charge2list[[i, 1]], charge2list[[i, 2]]},
   {i, 1, Length[charge2list]}];
newlist3pos = Table[{charge3list[[i, 3]], charge3list[[i, 1]], charge3list[[i, 2]]},
   {i, 1, Length[charge3list]}];
newlist4pos = Table[{charge4list[[i, 3]], charge4list[[i, 1]], charge4list[[i, 2]]},
   {i, 1, Length[charge4list]}];
newlist5pos = Table[{charge5list[[i, 3]], charge5list[[i, 1]], charge5list[[i, 2]]},
   {i, 1, Length[charge5list]}];
newlist6pos = Table[{charge6list[[i, 3]], charge6list[[i, 1]], charge6list[[i, 2]]},
   {i, 1, Length[charge6list]}];
```

- **Negative voltages (positively charged particles)**

The program below takes the SMPS data given as size distribution data as a function of DMA rod voltage, and obtains the corresponding size and charge distributions for q=(1, 2, 3, etc.).

```
Clear[voltagelist, datalist0, diameterlist, datalist, numberconcdata, Zplist, resultsfulllistqs]

voltagelist = Drop[rawdataneg[[1]], 1];
(* This extracts the voltages from the raw data: row #1 with the first
   element (blank entry) dropped. NOTE: voltage list must be absolute values!! *)
datalist0 = Drop[rawdataneg, 1];
(* Takes the raw data set and drops the first row. Gives
  rows with the particle diameter as the first element followed by the # of
  particles for each voltage. this gives Length(voltagelist)+1 row elements. *)
```

```
diameterlist = Table[datalist0[[i, 1]] * 10^-9, {i, Length[datalist0]}];
(* creates an array of just the diameters from the data set: row i,
column 1. Also converted to (m) from (nm) *)
datalist = Table[If[j == 1, datalist0[[i, j]] * 10^-9, datalist0[[i, j]]],
   {i, Length[diameterlist]}, {j, Length[voltagelist] +1}] ;
 (* Converts only the diameters (column 1) from (nm) to (m),
leaving all other elements the same *)
numberconcdata = Table[datalist[[i, j]], {i, 1, Length[datalist]}, {j, 2, Length[datalist[[1]]]}];
(* gives array of only the particle concentration data: rows 1-All & columns 2→All *)

TableForm[datalist, TableHeadings → {{}, Prepend[voltagelist "volts", "Particle Dia"]}];
(* Gives tabulated result for the "datalistgold" array with the "voltagelist" printed above *)

           (qsh + 0.5 * (qa - qm)) * Log[r2 / r1]
Zplist = - ---------------------------------------- ;
               2 × Pi × voltagelist × len
(* this computes the electrical mobility of the particles sampled by the first classifier
 using the classifier parameters. Negative sign corrects for the negative voltage,
since particle actually has positive charge. NOTE: Zplist is a matrix due to voltagelist *)

resultsfulllistqs = Map[selectlistqs[#] &, Range[2, Length[datalist[[1]]]]];
(* evaluates selectlistqs for all mobilities starting with the second
  column in datalistgold array (the first column is diameter values not # data)
  Note: the Map could only be carried out over one variable so the
    number of mobility elements was releated to the number of Zplist elements
     (i.e. Length[datalistgold[[1]]-1=Length[Zplist] or (40)-1=39 ) *)

totalresults = Map[totals[#] &, Range[1, 6]];
(* the above module is mapped over all charges (q) included in resultfulllistqs,
creating a size distribtution for each charge q *)


charge1list = Partition[Riffle[Flatten[totalresults[[1]]], 1, 3], 3];
charge2list = Partition[Riffle[Flatten[totalresults[[2]]], 2, 3], 3];
charge3list = Partition[Riffle[Flatten[totalresults[[3]]], 3, 3], 3];
charge4list = Partition[Riffle[Flatten[totalresults[[4]]], 4, 3], 3];
charge5list = Partition[Riffle[Flatten[totalresults[[5]]], 5, 3], 3];
charge5list = Partition[Riffle[Flatten[totalresults[[6]]], 6, 3], 3];
chargelisttot =
  Flatten[{charge1list, charge2list, charge3list, charge4list, charge5list, charge6list}, 1];
(* each charge list appends the number of charges to the list, all lists are then combined *)


datalist1neg = Table[{charge1list[[i, 1]], charge1list[[i, 2]]}, {i, 1, Length[charge1list]}];
datalist2neg = Table[{charge2list[[i, 1]], charge2list[[i, 2]]}, {i, 1, Length[charge2list]}];
datalist3neg = Table[{charge3list[[i, 1]], charge3list[[i, 2]]}, {i, 1, Length[charge3list]}];
datalist4neg = Table[{charge4list[[i, 1]], charge4list[[i, 2]]}, {i, 1, Length[charge4list]}];
datalist5neg = Table[{charge5list[[i, 1]], charge5list[[i, 2]]}, {i, 1, Length[charge5list]}];
datalist6neg = Table[{charge6list[[i, 1]], charge6list[[i, 2]]}, {i, 1, Length[charge6list]}];

newlist1neg =
  Table[{charge1list[[i, 3]], charge1list[[i, 1]], charge1list[[i, 2]]}, {i, 1, Length[charge1list]}];
newlist2neg = Table[{charge2list[[i, 3]], charge2list[[i, 1]], charge2list[[i, 2]]},
   {i, 1, Length[charge2list]}];
newlist3neg = Table[{charge3list[[i, 3]], charge3list[[i, 1]], charge3list[[i, 2]]},
   {i, 1, Length[charge3list]}];
newlist4neg = Table[{charge4list[[i, 3]], charge4list[[i, 1]], charge4list[[i, 2]]},
   {i, 1, Length[charge4list]}];
newlist5neg = Table[{charge5list[[i, 3]], charge5list[[i, 1]], charge5list[[i, 2]]},
   {i, 1, Length[charge5list]}];
newlist6neg = Table[{charge6list[[i, 3]], charge6list[[i, 1]], charge6list[[i, 2]]},
   {i, 1, Length[charge6list]}];
```

- **Neutral particles**

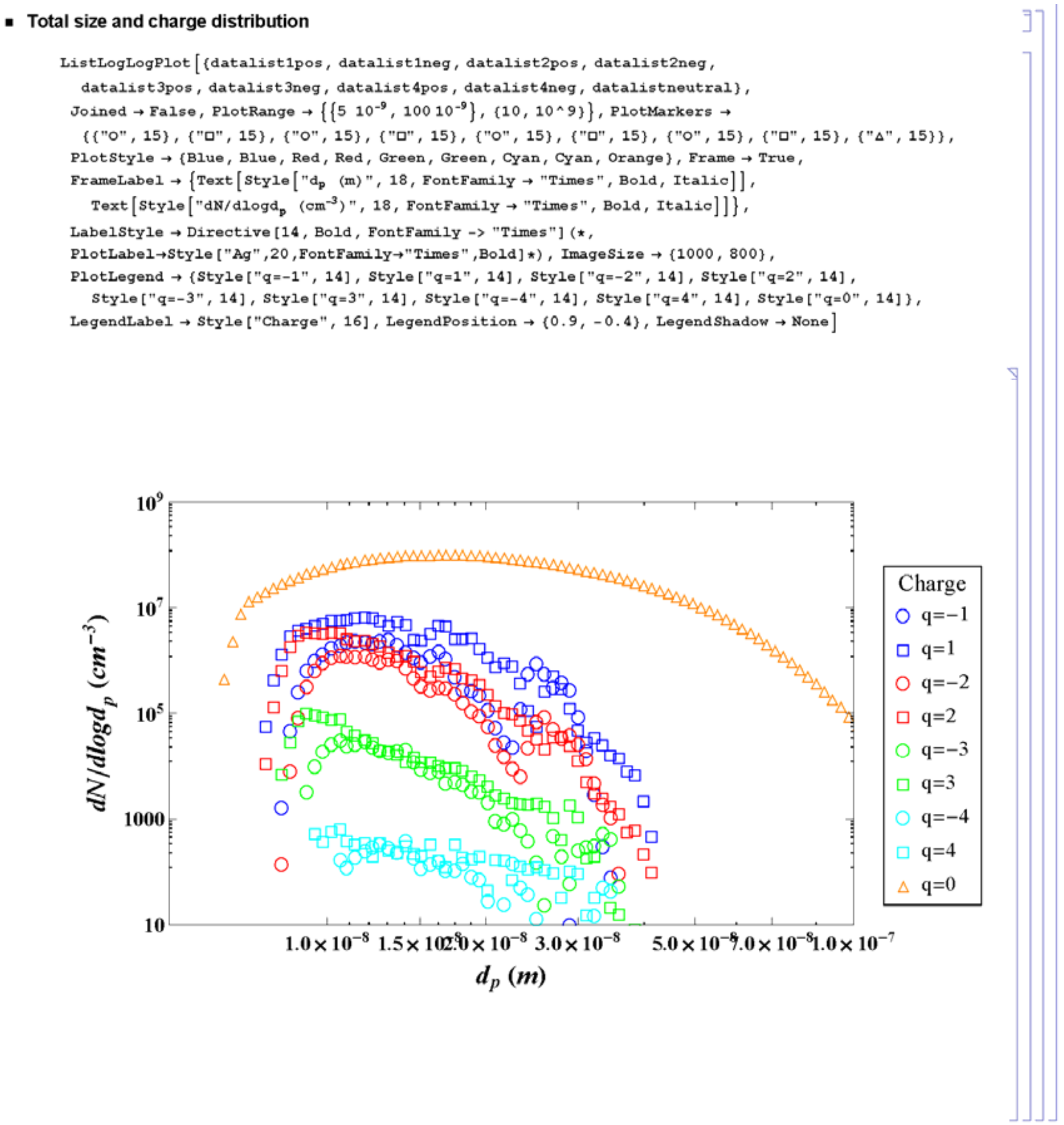

- **Total size and charge distribution**

```
ListLogLogPlot[{datalist1pos, datalist1neg, datalist2pos, datalist2neg,
  datalist3pos, datalist3neg, datalist4pos, datalist4neg, datalistneutral},
 Joined → False, PlotRange → {{5 10^-9, 100 10^-9}, {10, 10^9}}, PlotMarkers →
  {{"○", 15}, {"□", 15}, {"○", 15}, {"□", 15}, {"○", 15}, {"□", 15}, {"○", 15}, {"□", 15}, {"△", 15}},
 PlotStyle → {Blue, Blue, Red, Red, Green, Green, Cyan, Cyan, Orange}, Frame → True,
 FrameLabel → {Text[Style["d_p  (m)", 18, FontFamily → "Times", Bold, Italic]],
   Text[Style["dN/dlogd_p  (cm^-3)", 18, FontFamily → "Times", Bold, Italic]]},
 LabelStyle → Directive[14, Bold, FontFamily -> "Times"](*,
 PlotLabel→Style["Ag",20,FontFamily→"Times",Bold]*), ImageSize → {1000, 800},
 PlotLegend → {Style["q=-1", 14], Style["q=1", 14], Style["q=-2", 14], Style["q=2", 14],
   Style["q=-3", 14], Style["q=3", 14], Style["q=-4", 14], Style["q=4", 14], Style["q=0", 14]},
 LegendLabel → Style["Charge", 16], LegendPosition → {0.9, -0.4}, LegendShadow → None]
```

Figure E1. Example Mathematica program used to deduce charge-size distributions from measured data.

Appendix F

Charge-Size Distribution Results

Table F1

Charge-Size Distribution Results for Graphite, Gold, Silver, and Palladium

Particle charge	**Max concentration (#/cm^3)**	**Size Range (nm)**
Graphite		
0	4.62×10^{7}	7.37 – 225
−1	5.37×10^{7}	9.14 – 225
+1	3.25×10^{7}	9.47 – 225
−2	1.37×10^{7}	9.14 – 225
+2	1.47×10^{7}	9.47 – 225
−3	4.27×10^{6}	9.14 – 225
+3	8.37×10^{6}	9.47 – 225
−4	1.26×10^{6}	16.3 – 225
+4	5.15×10^{6}	13.6 – 225
−5	4.01×10^{5}	16.3 – 225
+5	3.37×10^{6}	13.6 – 225
−6	1.42×10^{5}	18.8 – 225
+6	2.29×10^{6}	15.7 – 225
−7	5.34×10^{4}	25.0 – 225
+7	1.59×10^{6}	16.3 – 225
−8	2.19×10^{4}	25.9 – 225
+8	1.12×10^{6}	18.8 – 225
−9	9.53×10^{3}	30.0 – 225
+9	8.07×10^{5}	20.9 – 225
−10	4.29×10^{3}	31.1 – 225
+10	6.07×10^{5}	20.9 – 225
Graphite (with aggregate particle correction)		
0	3.51×10^{7}	10.2 – 225
−1	4.54×10^{7}	10.2 – 225
+1	2.37×10^{7}	10.2 – 225
−2	1.17×10^{7}	10.2 – 225
+2	1.06×10^{7}	10.2 – 225
−3	3.89×10^{6}	10.2 – 225
+3	6.90×10^{6}	10.2 – 225
−4	1.20×10^{6}	16.3 – 225
+4	4.36×10^{6}	13.6 – 225
−5	4.06×10^{5}	16.3 – 225
+5	2.93×10^{6}	13.6 – 225
−6	1.46×10^{5}	18.8 – 225
+6	2.05×10^{6}	15.7 – 225
−7	5.70×10^{4}	25.0 – 225
+7	1.47×10^{6}	16.3 – 225
−8	2.44×10^{4}	25.9 – 225
+8	1.08×10^{6}	18.8 – 225
−9	1.06×10^{4}	30.0 – 225

+9	8.34×10^5	20.9 – 225
−10	4.84×10^3	31.1 – 225
+10	6.81×10^5	20.9 – 225
Gold		
0	1.08×10^8	6.15 − 217
−1	1.42×10^7	8.15 – 57.3
+1	3.59×10^7	7.37 – 68.5
−2	1.35×10^6	8.15 – 57.3
+2	4.35×10^6	7.37 – 68.5
−3	1.51×10^4	9.82 – 53.3
+3	1.12×10^4	8.20 – 68.5
−4	9.24×10^2	13.1 – 41.4
+4	8.20×10^3	10.9 – 66.1
−5	2.57×10^1	16.3 – 40.0
+5	3.24×10^2	11.3 – 66.1
Silver		
0	1.06×10^8	6.38 − 225
−1	2.53×10^6	8.20 − 35.9
+1	6.91×10^6	7.64 − 41.4
−2	1.26×10^6	8.20 − 35.9
+2	3.59×10^6	7.64 − 41.4
−3	3.15×10^4	9.14 − 35.9
+3	1.05×10^5	8.20 − 41.4
−4	3.83×10^2	10.6 − 35.9
+4	6.63×10^2	9.47 − 32.2
Palladium		
0	8.41×10^7	6.15 − 225
−1	1.73×10^7	8.82 – 85.1
+1	4.48×10^7	7.37 – 102
−2	1.62×10^6	9.14 – 85.1
+2	3.80×10^6	7.64 – 102
−3	6.51×10^4	15.1 – 76.4
+3	4.04×10^5	9.47 – 85.1
−4	3.00×10^3	16.3 – 76.4
+4	3.14×10^4	12.2 – 85.1
−5	2.83×10^1	25.0 – 59.4
+5	2.93×10^3	18.8 – 85.1